

2.114



SPACE OPTICS RESEARCH LABORATORIES, INC.

7 STUART ROAD CHELMSFORD, MASSACHUSETTS 01824
(617) 256-4511

LOW SCATTER LENS DESIGN/DEVELOPMENT

CONTRACT #NAS9-13561

(NASA-CR-134224) LOW SCATTER LENS
DESIGN/DEVELOPMENT (Space Optics Research
Labs., Inc.) CSCL 20F

N74-20322

G3/23 Unclass
35031

AUTHORS: Mr. Robert B. Gallipeau (S.O.R.L.)
Dr. Anthony Quesada (Consultant)

March 01, 1974

PRICES SUBJECT TO CHANGE

114

TABLE OF CONTENTS

	<u>PAGE</u>
A. <u>OPTICAL DESIGN</u>	1
I Introduction	1 - 3
II Final Design Procedures	3 - 4
III Detailed Technical Discussion	4 - 8
Table I	6
IV Final Performances Analyses	8 - 10
Table II	9
V General Conclusions	10 - 12
B. <u>SCATTERING ANALYSIS</u>	13
I Introduction	13 - 15
II The Total Energy Diffracted	16 - 19
III Computation of Δ for a Scratch, a Bubble, & Microscopic Irregularities	20 - 23
IV Distribution of Intensities	24 - 28
V Examples of Energy Distribution	29
VI Summary of Scattering Analysis	30 - 32
VII Effect of Bubble in Front Element, Directly Illuminated by Sun	33 - 37
Table III	34
VIII Comparison of 6-Element and 4-Element Designs	38 - 44
Table I	43
Table II & III	44

A. OPTICAL DESIGN

I INTRODUCTION

During the preliminary design stage of this investigation, approximately twenty different types of lens configurations were selected for the initial study effort. These lens systems were typical representations of three basic categories of physical arrangements:

1. Catadioptric - Consisting of both refracting and reflecting elements
2. Reflecting - Consisting mainly of first surface reflecting elements
3. Refracting - Consisting totally of refractive lens elements

The method used for selecting the optimum solution contained five essential criteria:

1. Image Quality - The blur circle diameters must not exceed 0.150 mm across the field of view considering 80% of the available energy.
2. Obscuration - The lens system should exhibit a minimum amount of energy losses due to physical obstructions within the system.
3. Distortion - The target objective for the system should be 3 arc minutes, or less, anywhere in the image format.
4. Collecting Area - The lens system should provide at least 18.3 cm² of collecting area for on-axis targets.

5. Physical Restrictions:

- a) System Envelope - The maximum dimensions of the package should not exceed a cylindrical volume of six inches diameter by six inches in length.
- b) Weight - The design goal was given as five pounds or less.

The following criteria were used as additional weighting parameters in selecting a lens configuration which would possess desirable attributes in terms of producing a suitable prototype model of the theoretical solution:

1. Material Considerations - High ultra-violet transmitting glasses, of low cost, ready availability, and good working characteristics would be needed.
2. System Sensitivity Factors - The final solution should possess relatively low insensitivity with respect to nominal optical fabrication tolerances and individual mechanical seating errors in the lens mount.
3. Ghost Image Locations - A suitable design would possess a minimum number of ghost images close to the final focal plane.

As was reported on in the first preliminary report there were fourteen individual lens designs that were brought to a point of semi-final completion. From these, only one solution exhibited outstanding performance characteristics in terms of the first five rating criteria. This particular system was a six element refracting design, operating at a

relative aperture of $f/1.0$ and possessing good image quality across the entire image format. The limiting factor in this design selection was the necessity of using rather high index materials. Since high refractive indexes usually indicates dense flint glasses of comparatively low ultra-violet transmission, or heavy lanthanum type crown materials which are expensive, it was realized that this particular solution would require careful study to insure the best material choices.

II. FINAL DESIGN PROCEDURES

There were many factors governing the final selection of appropriate materials for this solution. Since the specifications require high transmission in the low ultra-violet spectral region, only those glass types in the Schott catalog which gave values of 90% or greater, at 400 NM were considered useable. Therefore, the initial effort consisted of adjusting the nominal theoretical solution to accommodate the exact catalog values. Schott lists eighteen separate lanthanum type glasses. Of these only six possess refractive indexes of 1.7, or greater: LaK-8 (713556), LaK-10 (720504), LaKN-16 (734517), LaK-17 (788505), LaKN-18 (729542) and LaKN-19 (755531). The last two types are special order items only and should be avoided for volume fabrication systems. LaK-17 contains thorium and is four times more expensive than more conventional lanthanum glasses. Therefore, it was eliminated. LaKN-16 is twice as expensive and not manufactured as frequently as other glasses in this classification. Therefore, the final selection of LaK-8 was based on its lower cost, desirable Abbe dispersion value of 53.83 and its slightly better transmission value, over LaK-10, in the U-V region. Identical

procedures were followed in the selection of SF-1 and SF-19 for suitable materials. There is a wider choice of heavy flint materials, however, so these two glass types could be chosen quite selectively in terms of how closely they matched the theoretical glasses of the preliminary design solution. These flint materials, of course, were less expensive than the lanthanum glasses by a factor of about four times. However, there was no suitable low cost substitute for the lanthanum type crowns and they had to be used.

Upon completion of suitable optical material selection, the preliminary theoretical design values were then bounded so as to squeeze the solution towards the actual catalog values of the selected glass types. The optimization program uses all the lens variables, such as: lens radii of curvature, element center thicknesses and air spaces. Both damped least squares and ortho normal matrix inversion techniques are utilized in this optimization program to achieve rapid convergence of the final design solution.

III. DETAILED TECHNICAL DISCUSSION

As the optimization cycles progressed it became quite obvious that the image quality below 440 NM degraded very rapidly. This is quite typical when correction over a rather broad spectral range is attempted, particularly at fast relative apertures. Therefore, as mentioned in the earlier report, this obstacle was anticipated. There are very few optical materials which permit a lens system to be corrected down near 400 NM, especially when good quality is required in the red portion of the spectrum. The exact transition point could not be predicted prec-

isely since the tolerable blur circle diameter of 150 microns is quite modest and it was hoped that even at 420 to 430 NM, a satisfactory performance level could be attained. The dominant influence affecting the cut-off point for the low end of the spectrum was the fast operational speed of $f/1.0$. At this relative aperture, the lens radii are quite short which, in turn, produces higher order aberration contributions. These surface contributions must then be balanced by equally strong contributions of opposite sign, which produces strong zonal characteristics.

The system was also severely restrained by the requirement on the long back focus value of 1.00 inch. Ordinarily, in such a fast system, this working distance would be of the order of 10 to 20% maximum of the equivalent focal length, rather than the required 50%. As the design progressed then, there was a continual struggle to improve the image quality across the field and yet maintain the desired 1.00 inch distance.

A careful check was also maintained on the individual positive element edge thicknesses and negative element center thicknesses. Both these values had to be maximized to insure adequate ease in fabrication and sufficient strength in mechanical mounting to assure long life under operational conditions. The final lens prescription that evolved from this analysis is detailed in the Table I below:

TABLE 1

LOW SCATTER LENS SYSTEM: CONSTRUCTION DETAILS

<u>SURFACE NUMBER</u>	<u>RADII OF CURVATURE</u>	<u>VERTEX SEPARATIONS</u>	<u>GLASS MATERIALS</u>	<u>CLEAR APERTURE RADII</u>
1	Entrance Pupil	-2.7000		0.971
2	3.599	0.540	LaK-8	1.147
3	-6.109	0.004		1.092
4	1.844	0.633	LaK-8	0.895
5	4.251	0.156		0.640
6	-2.061	0.250	SF-19	0.636
7	0.999	0.179		0.553
8	Glare Stop	0.070		0.555
9	-2.680	0.200	SF-1	0.557
10	1.995	0.002		0.627
11	1.811	0.640	LaK-8	0.643
12	-1.236	0.004		0.695
13	1.509	0.380	LaK-8	0.624
14	21.849	1.004		0.557
15	Image Surface: Flat	-		-

NOTE: In order to achieve high volume productive capacity, the lens radii were constrained to equal 1.000 inch, or greater. This factor did not exert an unduly severe restraint upon the optical design.

The performance characteristics for this final optimized solution are shown in Fig. 1, 2 and 3. These are conventional ray intercept versus ray height in the entrance pupil plots, for each of three field angles. Fig. 1. is the information for the on-axis analysis, Fig. 2. for half-way out in the field, and Fig. 3. shows the image quality at the extreme edge of the field. In each set of these plots, there are three separate representations. The first, located at the top of the page and labeled SAG FAN Y, shows the Δy , or comatic type errors, for the sagittal fan of energy. The second plot, in the center of the page and labeled SAG FAN Z, gives the ΔZ , or skew errors, for the sagittal fan. These two plots are given only for the center to the edge of the pupil since the negative side of the data will be a mirror image of the positive side of the pupil aperture. The bottom plot provides the image errors for the meridional or tangential, energy fan. The total aperture, from a relative height of +1.0 to a relative height of -1.0, must be shown here since there is no inherent symmetry between the two halves of the pupil aperture. The main vertical divisions are the image errors directly, for any particular ray height in the entrance pupil, and are given in .010 mm steps. Three separate wavelengths are distinguished on each plot, indicated by L (for low index), M (for mean index) and H (for high index). In this instance, as mentioned previously, L = 0.55 microns, M = 0.4935 microns, and H = 0.45 microns.

An examination of Fig. 1. shows that essentially all the available energy is within a blur circle of about 0.080 mm diameter. Similarly, Fig. 2. which is for a position half-way out in the field, shows all

the energy is concentrated within a 0.085 mm diameter blur circle. Finally, Fig. 3., for the edge of the field, shows about the same degree of correction.

All these curves show the effect of very strong zonal errors which is quite typical of very fast optical systems. This necessity for balancing very strong opposing aberrations is usually the limiting factor in the level of image quality attained. For this case, the burden upon the optical design was intensified due to the enhanced working distance requirement and the extended spectral range coverage into the blue region.

IV. FINAL PERFORMANCE ANALYSES

The performance characteristics of this lens system in a more pictorial form in Plates #1 through # LVII. These plots give the exact physical shape of the blur circle pattern for each wavelength and each designated field angle. Seven discrete steps in the spectral range extending from 0.400 microns to 0.600 microns are given at six different field angles from 0.0 degrees out to 7.50 degrees, half-angle. The representations for the low blue region of 0.40 microns are included even though the lens system could not be corrected this far down into the blue region.

All the plots are initially scaled for one inch equals 0.005 mm. However, if the energy plots exceed this value then the program automatically scales the data to keep the total plot on the page. The

new scale is printed out at the top left hand position on the sheet. Plate I, for example, shows a scale factor of one inch equals 0.034630 mm. This is for a wavelength of 0.400 microns, at a field angle of 0.0 degrees, as shown. In this plot 100% of the available energy will be within 0.303 mm. Of course, the blur circle diameter becomes substantially smaller, as a lower energy concentration is considered. For example, if 75% of the available energy is considered, then the blur circle diameter becomes about 0.140 mm.

A total summary of all this data is given in Table II below.

TABLE II.
SPOT DIAGRAM ANALYSIS

FIELD ANGLE; SINE	λ	BLUR CIRCLE DIAMETER, mm. 100% ENERGY						
		0.4	0.45	0.475	0.500	0.525	0.550	0.600
0.000 ^o	0.000	0.303	0.126	0.088	0.066	0.058	0.062	0.063
	0.026105	0.313	0.133	0.095	0.089	0.074	0.074	0.066
	0.052210	0.332	0.150	0.111	0.086	0.072	0.071	0.091
	0.078316	0.361	0.146	0.105	0.109	0.109	0.107	0.086
	0.104421	0.351	0.153	0.132	0.112	0.099	0.093	0.101
	0.130526	0.0348	0.217	0.175	0.149	0.138	0.105	0.106

The above results show that the system is well corrected over the entire spectral range extending from 0.45 to 0.60 microns, even when considering the full 100% of the available energy. The performance at 0.40 microns is also within the allowed 0.150 mm. if about 80 to 90% of the available energy is considered. Therefore, in terms of the minimum weight package, the best available solution of suitable glass types, and considering reasonable restraints for manufacturing

ease, the final solution represents an optimum compromise of all the factors involved.

During the actual fabrication procedure for this lens system there would be a so-called melt adaptation required. This process is necessary because the actual refractive index of the manufactured glass could differ slightly from the catalog values used for the theoretical solution. In this melt adapting re-vision an attempt would also be made to extend the back focal length slightly to provide more working distance between the last surface of the lens barrel and the image plane. Even though this represents a difficult parameter to move, the performance of the lens is still comfortably within the 150 micron blur circle diameter allowance. Therefore, a slight increase might be possible.

V. GENERAL CONCLUSIONS

To a great extent the success or failure of this lens system will be largely dependent upon the reduction of the scattering effects, latent in the lens system. These effects will be produced by a variety of contributing factors as shown below:

1. Proximity of "ghost" image planes to the true focal plane.
2. Size and quantity of foreign inclusions within the glass volume, including bubbles, striae, and inhomogeneities.
3. Presence of surface defects such as:

- a. Sub-surface micro-fractures due to surface grinding techniques
- b. Surface scratches and digs
- c. Polishing streaks on the surface
4. Non-uniform optical coatings including sputters, stains, and pin-holes.
5. Surface dust particles and stains.

Under the first item above a detailed analysis was performed to determine the location of all ghost images due to internally reflected energy. Since the first set of energy reflecting pairs is most critical it is important that the reflected image formed by the first lens element is not located near the true image surface. As shown in the attached computer output the ghost image formed by the combination 3, 2 is located at 10.021 inches from the last vertex. This is well removed from the image plane and will not contribute any spurious image signal to the detector. The next ghost image of importance is formed by the pair 4, 3 and is located at 2.112 inches from the last vertex. This distance also is well removed from the true image surface. All other ghost images are considerably attenuated due to multiple reflections and would not need to be considered.*

The remaining factors on the above list pertain directly to the optical shop finishing techniques and to the perfection of the optical coating processes. Since the methods of optical fabrication technology

*Ref. Discussion on theoretical energy scattering - Dr. A. Quesada

represent especially advanced areas of skilled expertise by SORL optical shop technicians, the actual optical fabrication should present no unusual problem. SORL has achieved considerable success and background knowledge with the production of low scatter surfaces for the laser fusion industry using high energy lasers. However, the quality control of the coatings will demand painstaking attention. Inspection equipment must be designed to monitor the surfaces after coating and those which do not meet specifications imposed must be rejected and re-done.

The lens system, finally, must be assembled in a true, clean room environment where the atmosphere is micro-filtered to remove all contaminating dust particles. SORL does maintain an electronically filtered clean room for such assembly purposes.

B. SCATTERING ANALYSIS

I Introduction

Techniques to estimate the fraction of light scattering from very rough surfaces have been known for several decades (1). They are based on mathematical models that assume the phenomenon to be capable of description within the scope of geometrical optics, by combining statistical methods with estimates of the path differences of luminous rays that have been operated on by the irregularities of the rough surface. The experimental evidence that was available showed that, although consideration of the magnitude and number of irregularities led to a qualitatively acceptable interpretation of the scattering phenomenon, quantitative predictions were incorrect, particularly when the spatial distribution of scattered energy was desired. The need for closer agreement between theory and experiment led the early investigators to the conclusion that a theory from which acceptable quantitative estimates could be derived required that diffraction effects be taken into account. This requirement becomes mandatory when surface or refractive defects become very small and/or are few in number. Attempts to develop diffraction oriented theories have not been very numerous. To our knowledge, the earliest one is due to A. Marechal (2) who treated the problem in the light of the theoretical framework of Fourier methods described in detail by Duffieux (3). In the present work we shall extend some of the techniques introduced by Marechal to include explicitly the effects of off-axis geometry and to take into account the effects of microscopic inhomogeneities in refractive

elements. In agreement with references (2, 4, and 5), we shall be concerned primarily with optical surfaces of good quality, whose irregularities are small enough to make all deformations imposed upon a wave front small in comparison to the wave length. The results to be presented are of two types. We shall obtain expressions for total integrated energies and, later, we shall develop the expressions for the corresponding energy distributions. Detailed derivations of equations that are not directly concerned with the evaluation of those energy expressions will be relegated to appendices. Whenever it seems appropriate, we have applied the equations to the numerical evaluation of scattered energy ratios for conditions that may arise in practice, or for the establishment of order of magnitude estimates that can serve as guidelines to determine whether detailed computer evaluation of multiple integrals are necessary to improve precision to a satisfactory degree. The applicability of Fourier methods is a consequence of simplifying assumptions regarding the geometry of a system. When the conditions that allow the simplification are not met, it becomes necessary to use a more general formulation in which the diffraction integrals have to be evaluated either numerically, on high speed computers, or asymptotically, by means of methods such as Laplace's, Kelvin's, or Debye's. The particular choice is primarily dependent on the limits that appear on the integrals to be evaluated.

The next two sections are devoted to the development of the theory on the basis of Fourier methods. The extensions to the more general formulation is, in most cases, immediate.

11 The total energy diffracted

Suppose we have a refractive surface S , approximately flat, that creates small irregular deformations on the wave front. To compute the total energy diffracted, we shall imagine that a lens L is placed as in the following figure to transform the quasi-plane wave front into a nearly spherical front Σ having the same irregularities. To calculate the distribution of amplitudes at a point $P(x, y)$ of the focal plane of the lens, we shall use on the wave front the angular coordinates (α, β) , the angles that the direction of the line joining the origin with the point on the wave front makes with the planes xOz and yOz . The use of the angular coordinates simplifies the exponent of the phase function that appears in the diffraction integrals. Further simplification to transform the integrals into Fourier integrals requires that certain conditions be satisfied by the coordinates of the observation point on the focal plane or near the focal plane of L . These are discussed in appendix 2. We know that under the conditions that allow writing the integrals as Fourier integrals (6) it is possible to express the amplitude of the electric field $E(x, y)$ at the point $P(x, y)$ by Huygens' principle, according to which if $F(\alpha, \beta)$ is the amplitude distribution on a sphere centered at 0, then

$$E(x, y) = \frac{iR}{\lambda} \iint_{\Sigma} F(\alpha, \beta) e^{ik(\alpha x + \beta y)} d\alpha d\beta$$

(1)

where R is the radius of the reference sphere and $k = 2\pi/\lambda$.

If the wave front is deformed by an amount Δ with respect to the reference sphere the amplitude on the sphere is of the form $E_0 e^{ik\Delta}$, where E_0 is a constant over the wave front. If we now postulate that Δ is small in comparison to λ , we can write

$$e^{ik\Delta} \approx 1 + ik\Delta$$

(2)

We can choose the radius of the reference sphere in such a way that the mean value of Δ vanishes ($\bar{\Delta} = 0$). In these circumstances, the amplitude distribution over the aperture is the sum of two terms: a) a uniform amplitude $F_1 = E_0$ and b) a fluctuating amplitude of mean value zero $F_2(\alpha, \beta) = ik E_0 \Delta(\alpha, \beta)$.

Consequently, the resultant field $E(x, y)$ is the sum of two terms. The field E_1 is the field diffracted by the aperture utilized. It is very small, except near the geometrical image of the source, within a domain whose area varies inversely as the area of the aperture. We shall be more interested in the field E_2 , whose amplitude generally

decreases far more slowly. The defects represented by the function F_2 are, in general, small in extent by comparison with the extent of the aperture. Consequently, they diffract light into an area far more extensive than the area over which E_1 has appreciable magnitude. To compute the energy diffracted, we must introduce a more precise definition. We shall adopt, with Marechal, a definition based on the integral of the flux due to the amplitude E_2 . Using Parseval's theorem, which expresses energy conservation, we can write this energy as proportional to

$$\iint |E_2(x,y)|^2 dx dy = R^2 \iint |E_2(\alpha,\beta)|^2 d\alpha d\beta \quad (3)$$

which, in view of the definition of F_2 is equivalent to

$$R^2 R^2 E_0^2 \iint_{\Sigma_1} \Delta^2 d\alpha d\beta \quad (4)$$

This integral is recognized as the mean square value of Δ . It is convenient to introduce the relative energy scattered, by division of the above expression by the total energy, which equals $E_0^2 R^2 \iint_{\Sigma} d\alpha d\beta$. Then,

$$\rho = \frac{k^2 \iint_{\Sigma} \Delta^2 d\alpha d\beta}{\iint_{\Sigma} d\alpha d\beta} = \left(\frac{4\pi^2}{\lambda^2}\right) \overline{\Delta^2} \quad (5)$$

Thus, the energy scattered over the image plane, expressed as a fraction of the total energy, is proportional to the mean square value of the optical path-length error Δ . We may recall that a similar result is obtained in connection with the loss of illumination at the center of a diffraction pattern when small aberrations are introduced. It is known that in this case, the relative loss of illumination is precisely equal to $k^2 \overline{\Delta^2}$ and that the energy taken away from the central spot is distributed over the focal plane.

III. Computation of Δ for a scratch, a bubble, and microscopic irregularities.

Let us apply Eq. (5) to an irregularity in the shape of an ellipse. Limiting cases are clearly a narrow straight groove that can simulate a scratch and a crater-like depression that may be representative of a flaw in an anti-reflection coating. In line with the discussion of section 2.1, the dimensions of the ellipse are small in comparison to the effective area of the domain of integration. From appendix 1, we have the Δ values

$$\Delta = 2n\epsilon w \sin i \quad \text{for a reflector, and}$$

$$\Delta = (\cos r - n \cos i) \epsilon \quad \text{for a refractive}$$

surface. Since the dimensions are small, the angles i and r are essentially constant. Also, strictly speaking, to satisfy the condition $\bar{\Delta} = 0$, we should modify the definitions of Δ above. However, since the area, A , of the irregularity is such that $\Delta \ll \Sigma$, where Σ is the area of the aperture, the correction to ϵ is of order A/Σ and, therefore, entirely negligible. We then have

$$\begin{aligned} \bar{\Delta}^2 &= \iint_{\Sigma} \Delta^2 d\alpha d\beta = 4\Delta^2 \int_0^{A/\beta} d\beta \int_0^{\left(\sqrt{1-\frac{\beta^2}{A^2}}\right) \Delta n} d\alpha \\ &= 4\Delta^2 (\Delta n) \int_0^{A/\beta} \sqrt{1-\frac{\beta^2}{A^2}} d\beta \\ &= 4\Delta^2 \cdot \frac{1}{2} (A n) (A/\beta) \end{aligned}$$

Hence,
$$P = \frac{2\pi (1-n) (A/A) \Delta^2}{\Omega} \left(\frac{2\pi}{\lambda}\right)^2$$

where Ω is the solid angle subtended by the aperture at the focal point. This equation can be modified to read

$$P = \frac{2\pi ab \Delta^2}{A} \left(\frac{2\pi}{\lambda}\right)^2$$

where a and b are the semi-axes of the elliptical irregularity and A is the effective area of the aperture. For a refractive surface, for example, we have in the worst possible case

$$\Delta = (1-n) \epsilon$$

Therefore,

$$P = \frac{2\epsilon(n-1)^2 [\text{volume of irregularity}]}{A} \left(\frac{2\pi}{\lambda}\right)^2$$

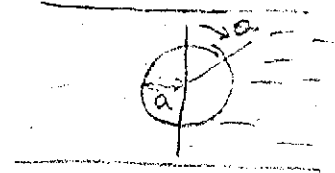
For an axi-symmetric system whose effective aperture is defined by an f-number we can write

$$P = \frac{8\pi(n-1)^2 (\text{area of irregularity})}{(\text{f-number})^2} \left(\frac{\epsilon}{\lambda}\right)^2$$

In other words, the fraction of the energy scattered is proportional to the area of the irregularity, to the square

of the depth of the irregularity measured in wave lengths and inversely proportional to the effective area of the aperture. For a bubble of radius a inbedded in a refractive surface, we have approximately,

$$\Delta = 2(n-1) a \cos \theta$$



and

$$P = \frac{3\pi (n-1)^2 a [\text{volume of bubble}]}{A} \left(\frac{2\pi}{\lambda}\right)^2$$

Finally, for microscopic irregularities, let us consider a very simple model in which they are distributed in such a way as to cause a random error in the mean position of the wave front, for which the probability of finding a value of ϵ between ϵ and $\epsilon + d\epsilon$ is given by the expression

$$\frac{d\epsilon}{\sqrt{2\pi} (\epsilon \Delta n)^2} e^{-\left(\frac{\epsilon}{\epsilon \Delta n}\right)^2}$$

where t represents the thickness of the refractive element and Δn is a representative value of the index fluctuation in the medium. Taking the ensemble average, we find that with N the average number of volume elements with distinct values of the index encountered by a luminous ray.

$$\langle \overline{\Delta^2} \rangle = \Omega (\pm \Delta n)^2 \frac{1}{N}$$

Hence,

$$P = \frac{4\pi^2}{N} \left(\frac{\pm \Delta n}{\lambda} \right)^2$$

Since Δn can be as small as 10^{-6} , the energy loss from this source of irregularities is generally very small, as N is of the order of 1000/cm.

IV Distribution of Intensities.

To characterize the intensity distribution, we must construct the function

$$D(x, y) = |E_2(x, y)|^2 \quad (6)$$

The function $E_2(x, y)$, by virtue of Huygens' principle can be expressed as a Fourier transform of the function $F_2(\alpha, \beta)$. Since, in general, the function $F_2(\alpha, \beta)$ is random, it may appear that we can only calculate the mean value of its square. This, however, is not the case. It is possible to calculate the energy distribution because this energy distribution is the Fourier transform of the correlation function of F_2 . Recall that

$$E_2(x, y) = \frac{iR}{\lambda} \iint_{\Sigma_1} F_2(\alpha, \beta) e^{ik(\alpha x + \beta y)} d\alpha d\beta \quad (7)$$

The energy distribution is $|E_2(x, y)|^2$, a function whose Fourier transform may be found by means of the correlation function, that is, its own Fourier transform. The derivation is straight-forward and may be found, for example, in reference (7). The result can be stated as follows:

If $G(\xi, \eta)$ is the two-dimensional Fourier transform of $g(x, y)$, then

$$\mathcal{F}\left\{\iint g(x, y) g^*(x-\xi, y-\eta) dx dy\right\} = |G(\xi, \eta)|^2 \quad (8a)$$

and similarly,

$$\mathcal{F}\{|g(x, y)|^2\} = \iint G(\xi, \eta) G^*(\xi+\xi', \eta+\eta') d\xi d\eta \quad (8b)$$

where the script \mathcal{F} stand for "the Fourier transform of."

Let us apply Eq. (8b) to $E_2(x, y)$, identifying $g \leftrightarrow E_2$, and denoting the resultant transform $d(\xi, \eta)$. We have

$$d(\xi, \eta) = R^2 \iint_{\Sigma} E_2(\alpha, \beta) E_2^*(\alpha + \xi/2, \beta + \eta/2) d\alpha d\beta \quad (9)$$

Or,

$$d(\alpha', \beta') = k^2 R^2 E_0^2 \iint_{\Sigma} \Delta(\alpha, \beta) \Delta(\alpha + \alpha', \beta + \beta') d\alpha d\beta$$

Note that in Eq. (9), we have introduced the non-dimensional displacements $\xi/2$ and $\eta/2$. This is necessary to preserve the dimensional homogeneity of the arguments of

the functions $\Delta(d, \beta)$ and $\Delta(d + d', \beta + \beta')$. It is sometimes convenient to write the correlation integral in the form

$$\iint \Delta(\alpha, \beta) \Delta(\alpha + \alpha', \beta + \beta') \Omega d\alpha d\beta = \Omega \bar{\Delta}^2 \Psi(\alpha', \beta') \quad (10)$$

where Ω is the solid angle subtended by the aperture and $\Psi(\alpha', \beta')$ is a normalized correlation function

$$\Psi(\alpha', \beta') = \frac{\Delta(\alpha', \beta')}{\Delta(0, 0)}$$

Using Eq. (10) establishes a direct link between the energy distribution, its Fourier transform, and the mean square value of the path length errors that we calculated in section 2.1. Eq. (10) indicates that if a defect covers an appreciable portion of the aperture (for example, an error of figure) the correlation function decreases slowly. In the case the functions $\Delta(d, \beta)$ and $\Delta(d + d', \beta + \beta')$ are nearly identical and the integral of the product is approximately equal to $\Omega \bar{\Delta}^2$. If, on the other hand, $\Delta(\alpha, \beta)$ varies rapidly, the two functions contribute to the integral only over a limited range of displacements. In either case, the energy distribution, $|E_2(x, y)|^2$ is obtained by inversion of the transform, Eq. (10). That is,

$$D(x, y) = \iint \Delta(\alpha', \beta') e^{-\frac{2\pi i}{\lambda}(\alpha' x + \beta' y)} d\alpha' d\beta' \quad (11)$$

or equivalently,

$$D(x, y) = \frac{k^2 R^2 E_0^2 \Omega \bar{\Delta}^2}{\lambda^2} \iint_{-\infty}^{\infty} \psi(\xi, \eta) e^{-2\pi i \left(\frac{x\xi}{\lambda} + \frac{y\eta}{\lambda} \right)} d\xi d\eta$$

$$= 4\pi^2 R^2 E_0^2 \Omega \frac{\bar{\Delta}^2}{\lambda^4} \bar{\Phi} \left(\frac{x}{\lambda}, \frac{y}{\lambda} \right)$$

(12)

where $\bar{\Phi} \left(\frac{x}{\lambda}, \frac{y}{\lambda} \right)$ denotes the double integral inverse transform.

This expression suggests a simple way of measuring the energy distribution. Suppose we can determine the mean square value of Δ and can measure the ratio of the flux $D(x, y)$ to the total flux ($= R^2 \Omega E_0^2$) at given locations, but as functions of the wave length. Suppose that subsequently we construct the curve representing $\left\{ \frac{\lambda^4}{R^2 \Omega E_0^2} D(x, y) \right\}$ as a function of x/λ and y/λ . According to Eq. (12), this curve represents the product $\bar{\Delta}^2 \bar{\Phi}$. Since $\bar{\Delta}^2$ is a very weak function of the wave length, upon division by $\bar{\Delta}^2$ and subjecting the function $\bar{\Phi}$ to the condition that its Fourier transform is equal to unity when $\alpha = \beta = 0$, there results the function $\bar{\Phi} \left(\frac{x}{\lambda}, \frac{y}{\lambda} \right)$. The spatial energy distribution for a given wave length follows immediately by a simple change of variable. To avoid interference from the intense direct images, the experiment should be conducted with a black hole to eliminate the contribution from the direct images. The construction of such a device is described in reference (8).

The decrease in illumination is again a Gaussian function. Again, these examples show that large scale defects, such as figure errors, lead to large values of w and, consequently, energy distributions that fall off rapidly. On the contrary, when the defects are small, the correlation has short range and the diffracted light is spread out widely over the focal plane.

V Examples of Energy Distribution.

Let us consider the case of an irregularity of rectangular shape, of dimensions w and l , simulating a small scratch. In this simple case, the normalized correlation function is

$$\psi(\alpha, \beta) = \frac{wl}{\pi^2} \left(\frac{\sin(\frac{\pi w \alpha}{\lambda})}{\frac{\pi w \alpha}{\lambda}} \right) \left(\frac{\sin(\frac{\pi l \beta}{\lambda})}{\frac{\pi l \beta}{\lambda}} \right) \quad |\alpha| \leq \frac{\lambda}{w} \quad |\beta| \leq \frac{\lambda}{l}$$

$$= 0 \quad \text{elsewhere}$$

and, therefore,

$$\Phi\left(\frac{x}{\lambda}, \frac{y}{\lambda}\right) = \frac{\sin^2\left(\frac{\pi w x}{\lambda}\right) \left(\frac{w}{\lambda}\right) \cdot \sin^2\left(\frac{\pi l y}{\lambda}\right) \left(\frac{l}{\lambda}\right)}{\left(\frac{\pi x}{\lambda}\right)^2 \left(\frac{\pi y}{\lambda}\right)^2}$$

As a second example, let us consider an autocorrelation function of Gaussian character. We might expect such a correlation function to describe the wave front distortions introduced by microscopic inhomogeneities. Let, then,

$$\psi(\alpha, \beta) = e^{-\frac{\pi^2 w^2}{\lambda^2} (\alpha^2 + \beta^2)}$$

where w is a parameter that fixes the scale of correlation and, in general, can be interpreted as indicating that the irregularities of the wave front are seen from the origin 0 as subtending an angle of order w . The function $\Phi\left(\frac{x}{\lambda}, \frac{y}{\lambda}\right)$ is in this case

$$\Phi\left(\frac{x}{\lambda}, \frac{y}{\lambda}\right) = \pi w^2 e^{-\frac{\pi^2 w^2}{\lambda^2} (x^2 + y^2)}$$

VI SUMMARY OF SCATTERING ANALYSIS

The theory that was developed to deal with levels and spatial distribution of scattered light can be applied with little modification to define limits on the number and extent of scattering centers that may be tolerated in the tracker optics. It is important to bear in mind that a theoretical study can very effectively provide tolerance criteria to be met by the optical designer, rather than predict in detail how a system will perform. The latter requires that a system already in existence be examined to determine the type, magnitude and distribution of bulk and surface defects in each component. If this is known then the theory can predict how much light will be scattered and how will the energy be distributed. Theoretical considerations are also useful in interpreting the results of scatter measurements on a system being tested. This is particularly true of the stretch correlation, that provides outputs that are invariant under changes of scale.

When the theory is applied to determine tolerances it becomes apparent that the most critical parts of the system are the front elements. This is because the intensity of the scattered light reaching the image plane is proportional to the flux incident on the irregularities responsible for diffracting the light and introducing distortion of the wavefront. The effect of the irregularity itself, as far as diffraction effects are concerned, is the same regardless of where that irregularity is located. It leads to distortions of the wavefront characteristic of the type and dimensions of the irregularity. A small bubble, for example, that diffracts 1/10 of 1% of the light may be tolerated in an inner element shielded by geometry from direct sun light at all angles of interest. The same bubble would totally

destroy the system performance if present in the front element under conditions that allow exposure to direct sun light. In this case, even the fact that the distribution of scattered light will in general be oriented at some angle with respect to the axis of the system would not be sufficient to compensate for the direct effect of incident flux. The incident flux is generally strong enough to cause an intolerable loss of contrast in spite of the small fraction of side scattered light that reaches the image plane.

When the equations were specialized to account for effects of small bubbles it was found that the front elements have to be essentially bubble free. Although the equations were used to define some limiting upper size for a bubble, they may be interpreted also as indicators of how many smaller bubbles can be allowed. The trade-off is not immediate because it must be recalled that even though a small bubble is responsible for a small distortion of the wavefront, the light that it scatters in the forward direction is spread over a much wider solid angle that would be the case if the size of the bubble is allowed to increase. Reference to the table on page 14 is necessary to estimate how the angular factors are to be changed when the bubble size is decreased.

A similar argument can be used to estimate the effects of surface defects. If the equations applicable to a scratch are used, we find that in the worst case no scratch of depth of order of the wavelength and longer than a few millimeters can be tolerated for the front surface or any surface that may be illuminated directly by the sun.

The worst case corresponds to a scratch oriented in a direction that will cause maximum spread of the diffracted light. It is important to remember that the quality of the surface finish or the quality of a coating can be evaluated in a variety of ways. For the small defects that we have considered electron microscopy, phase microscopy, dark field light microscopy and ellipsometry are suitable. For larger surface areas phase contrast and knife edge tests can be used. The measurements by any of these techniques can be used as inputs to the formulation that has been developed, to confirm that irregularities have been kept below the limits needed to meet performance specifications.

From the literature references, these are 4 main points which require special attention in terms of securing low scattering in lens systems. They are:

1. For a multiple lens element system the effect of flare is less at higher relative apertures than lower apertures.
2. For extended self-luminous objects, such as the horizon, the magnitude of the flare is proportional to the number of air-glass interfaces and not determined by the relative aperture.
3. In designing lens systems for low scatter applications, ghost reflected images adjacent to the image plane must be scrupulously avoided.
4. Good optical coatings do reduce the absolute magnitude of scattered energy, but porous films will slightly increase the amount of scattered energy.

VII EFFECT OF BUBBLE IN FRONT ELEMENT, DIRECTLY ILLUMINATED BY SUN

Eg's. (3) and (6) of Part I can be used to determine the effect of a small bubble in the front element of the proposed systems, when illuminated by direct sunlight falling on that element at an angle beyond the field of view. Several simplifying assumptions will be introduced, but in every case the simplification will be chosen in such a way as to produce 'worst' effects. This way we obtain criteria that, if met, will insure proper performance of the system.

Since the correlation function will in every case be analogous to the first example in section 3.2, the worst case can be approximated by distributing the total energy evaluated from eg. (3) over solid angles bounded by annular areas of radii equal to the distances corresponding to consecutive zeros of the function

$\sin \frac{\pi x}{\lambda} = \frac{\omega}{R}$. We shall identify ω with the radius of the bubble. It is convenient to express the argument of this function in terms of angular quantities measured from the direction of the incident light. The zeros, then, occur at angles θ_η such that,

$$\pi \frac{\omega}{\lambda} \tan \theta_\eta = \eta\pi \quad \eta = 1, 2, 3, \dots$$

or

$$\tan \theta_\eta = \frac{\eta\lambda}{\omega} \quad (1)$$

Values of θ_η for $\eta = 1, 2, 3, 4$ are given in the following table for a large range of values of $\frac{\omega}{\lambda}$.

TABLE III.

ω/λ	θ_1	θ_2	θ_3	θ_4
0.1	84.3°	87.1°	88.1°	88.6°
0.5	63.4	76	80.5	82.9
1.0	45	63.4	71.6	76
1.5	33.7	53.1	63.4	69
2.0	26.6	45	56.3	63.4
3.0	18.4	33.7	45	53.1
5.0	11.3	21.8	31	38.7
10.0	5.71	11.3	16.7	21.8
20.0	2.9	5.71	8.5	11.3
50.0	1.15	2.29	3.43	5.71
100.0	0.57	1.15	1.71	2.29
200.0	0.29	0.57	.86	1.15

The normalized peaks of energy density within each one of the areas bounded by zeros are 1, 0.047, 0.0034 and 0.0024, respectively.

From eq. (3), we find that the total energy scattered by the bubble is,

$$E_B = C R^2 k^2 E_0^2 (\bar{\Delta}^2)$$

where E_0 is the amplitude of the E-field and $C E_0^2$ can be taken as the energy density of the incident light.

Now, according to eq. (3) and the table shown before, the smaller bubbles scatter little light, but the scattering is over a very wide angle. On the other hand, the large bubbles scatter far more energy, (large $\bar{\Delta}^2$) but that energy is concentrated in the forward direction and relatively little is deflected to the sides. For example, when the bubble size is of the order of 10λ , the first zone extends to

less than 6° from the direction of incidence. Letting f be the attenuation factor due to angular effects we can then write:

$$p = \frac{\text{Energy density of scattered light in direction of } n\text{-th maximum}}{\text{Energy density of incident light}}$$

$$= \frac{1}{\pi} \left(\frac{2\pi}{\lambda} \right)^2 \left(\frac{\omega}{\lambda} \right)^2 \frac{1}{\Delta^2} f \quad (2)$$

If p is to be less than some small fraction E we must have

$$16\pi \left(\frac{\omega}{\lambda} \right)^6 \frac{\lambda^2 n_2^2}{R_o^2} f < E$$

or

$$\left(\frac{\omega}{\lambda} \right) < \frac{E}{16\pi f} \frac{1}{\lambda} \frac{R_o}{(n-1)} \quad (3)$$

The light that is scattered is allowed to pass through other elements of the system. When the angle of scattering is such that the fraction f reaches the focal plane, a further weakening of intensity takes place because the front element in general will not be in focus.

The decrease in intensity can be estimated when the position of the image plane for the bubble is known. The problem is similar to that encountered when one computes the flare of a system due to secondary reflections of air-glass interfaces. In this case, it is known* that the amount of flare light is proportional to the square of the f /number of the system and is inversely proportional to the (distance)²

*See, for example, Kuwabara, G., J. O. S. A., 43, 53 (1953).

of the secondary image from the focal plane. The latter effect is more serious and in designing an optical system it is desirable to avoid any pair of reflecting surfaces which produce a reflection image in the vicinity of the image plane. For the 6-element system, based on the figures obtained for the position of secondary image planes at normal incidence, we estimate that the reduction is of the order of 10. In general, we can call this factor f_1 and write instead of eq. (3)

$$\frac{\omega}{\lambda} < \frac{E}{16\pi f f_1} \quad \frac{R_o}{\lambda (n-1)} \quad \frac{1/6}{1/3}$$

If $\lambda = .5 \times 10^{-4}$ cm, $n = 1.5$, $R_o = 3$ cm, $E = 10^{-5}$,
 $f = 0.001$, $f_1 = 0.1$

$$\frac{\omega}{\lambda} < \sim 20$$

This means that bubbles in the first 2 elements must be essentially absent. The last condition may be relaxed somewhat, by recalling that the derivation of eq's. (3) and (6) required the wavefront distortion to be small. For bubbles $\sim 10 \lambda$ this is not strictly true and a more geometrical approach indicates that most of the scattering is forward, with edge effects superimposed on it, and amounting to a fraction proportional to some effective volume of the edge as compared with the entire bubble.

Equally important is the problem associated with anti-reflection coatings for the first 2 elements. Coatings are effective in reducing the flare caused by reflected light, but one must be very careful to

have coatings very homogeneous. Porous films enhance slightly the scattered light and tend to reduce contrast in the vicinity of a bright image.

VIII COMPARISON OF 6-ELEMENT AND 4-ELEMENT DESIGNS

Since a fractional rejection level of 10^{-5} will attenuate sunlight to the equivalent of a uniform background brightness of 0.1 foot-lambert, we shall examine the expected performance of the systems in terms of fractional rejection levels. The same criterion will be used for other sources such as the full moon or the earth's sunlit horizon. For conversion, it is convenient to use the fact that a star of visual magnitude 0, corresponds to illumination outside the earth's atmosphere of 2.65×10^{-10} lumens/cm². Thus, the full moon, with an equivalent visual magnitude of -12.70, leads to an illumination of 3.2×10^{-5} lumens/cm². The effect of the full moon, as far as incident flux on irregularities is concerned, is then nearly 300,000 weaker.**

The computations that follow were carried out under the assumption that glasses will be specified, at least for the first two elements of each system, which will have:

- a) Homogeneity: H2, that is, $\Delta n = \pm 5 \times 10^{-6}$
- b) Bubble Group 0, that is, total bubble cross-section in mm²/100cc volume of glass between 0 and 0.029. For the calculation, we require selection of the glass to have no bubble $> 60\mu$ and it will be assumed that smaller bubbles that may be present will have

**Allen, C. W., Astrophysical Quantities, U. of London, Athlone Press (1963) (pg. 145).

a maximum cross section of $0.015 \text{ mm}^2/100\text{cc}$ with a mean size approximately 20λ .

The volumes of the first two elements for the two systems were estimated to be 30cc and 27cc for the 6-element system and 9.1 and 7.2cc for the 4-element system.

For these circumstances, we can apply the equations developed in Part I of the theoretical analysis and construct Table I for the cases where the sources are outside the field of view.

These levels are comparable to the total values measured for good coronagraph lenses where (for those lenses not limited by fluorescence) the fraction of solar light scattering was between 1.2×10^{-6} and 5.7×10^{-6} (See Newkirk and Bohlin, App. Optics, 2, 131, 1963).

For the case of the full moon within the field of view, we have similar results. The most serious effect is due to the small angular deviations that we must now consider and the possibility of involving all elements of the system.

Since, however, the incident flux due to the full moon is some 300,000 weaker, in spite of the requirement for the equivalent background brightness to be 0.05 foot-lambert, the changes in the factors shown in Table II as compared with Table I are well within the 10^5 factor

that the weaker source and equivalent background allow.

Thus, either system will satisfy this specification.

Again, we emphasize that the figures represent worst cases.

A similar analysis for the case of the earth's sunlit horizon within the field of view shows that the specification can be met at angles of about 3° away from the edge of the horizon image. At closer angles, the presence of bubbles in the size range 20λ to 50λ may lead to areas where the specification is violated.

Ray tracing was used to determine the location of secondary image planes and to estimate the effects of the secondary images as sources of unwanted stray light. Assuming the reflectivity of air-glass interfaces to be of the order of 1%, we can summarize the results in Table III.

When the full moon is within the field of view spurious, images may be formed with illuminations in the image plane as bright as 6.4×10^{-8} lumens/cm² and 1.6×10^{-7} lumens/cm² (for 6-element and 4-element systems, respectively).

A fourth magnitude star having its energy distributed within 12arc minutes square field of view corresponds to an illumination of 2×10^{-6} lumens/cm² for the 6-element system and $.8 \times 10^{-7}$ lumens/cm² for the 4-element system.

-40-

PRECEDING PAGE BLANK NOT FILMED

40

We, therefore, have signal to noise ratio of

For the 6-element system:

$$S/N = \frac{2 \times 10^{-6}}{6.4 \times 10^{-8}} = 30$$

For the 4-element system:

$$S/N = \frac{.8 \times 10^{-7}}{1.6 \times 10^{-7}} = 1/2$$

which shows the 6-element system as a more promising system in this respect also.

TABLE I

MAXIMUM FRACTION OF INCIDENT INTENSITY SCATTERED

SYSTEM	ANGLE	DUE TO BUBBLES	DUE TO BULK INHOMOGENEITIES	DUE TO SURFACE DEFECTS* (PER DEFECT)
6-Element	30°	1.6×10^{-6}	3×10^{-7}	10^{-6}
	16°	4×10^{-6}	7.5×10^{-7}	10^{-6}
4-Element	30°	5×10^{-6}	1.5×10^{-7}	10^{-6}
	16°	1.2×10^{-5}	4×10^{-7}	10^{-6}

* EACH DEFECT EQUIVALENT TO A MICROSCRATCH OF DEPTH λ ,
 WIDTH = 1 MICRON AND LENGTH = 1000 MICRONS IN WORST
 POSSIBLE ORIENTATION (i.e. ANGULAR FACTOR = 1).

TABLE II

MAXIMUM FRACTION OF INCIDENT INTENSITY SCATTERED

SYSTEM	DUE TO BUBBLES	DUE TO BULK INHOMOGENEITIES	DUE TO SURFACE DEFECTS (PER DEFECT)
6-Element	6×10^{-3}	3×10^{-4}	10^{-6}
4-Element	10^{-2}	10^{-4}	10^{-6}

TABLE III

SPURIOUS IMAGE REJECTION

SYSTEM	AT 16°	AT 30°	AXIALLY
6-Element	Rays do not reach image plane	Rays do not reach image plane	$< 2 \times 10^{-3}$ for reflections due to 1st two elements
4-Element	$< 10^{-3}$	$< 10^{-3}$	$< 5 \times 10^{-3}$ for reflections due to 1st two elements

C. Fabrication Details

I. General Fabrication Summary

The complete specifications covering the optical fabrication tolerances are itemized in Table I. Most of these values are rather modest and easily held. However, some of the tolerances pertaining to individual element wedge, and lens centering error, are severe and must be carefully controlled. There is also one air space tolerance value which may require special assembly adjustment in order to obtain peak theoretical performance.

II Glass Material Selection

The particular glass materials chosen for this design were dictated by the design requirements discussed in the previous sections. However, the quality is determined by specifying "Schlieren Grade", PH4 with Special Bubble Selection. This insures that the variation in inhomogeneity will be of the order of $\pm 1 \times 10^{-6}$ within each blank, stress birefringence $\leq 3-4$ nm/cm and maximum inclusions (i.e. bubbles) of 0 - .029 cross section per 100 cc.

III Distortion Characteristics

The general distortion characteristics of the lens system are summarized in Table II. These values were

obtained directly from the computer print-out of spot diagrams giving the image centroid heights. The tolerance value of 3arc minutes for distortion was then converted directly into the allowed linear displacement value of 0.044mm. Then, the calculation of the residual distortion in the lens system was derived directly from the value in the table.

IV Transmission Characteristics

Table III shows the given catalog values of nominal internal transmittance values for the selected glass types. These glasses all show high values of transmittance at 400 nm, which is primarily why they were chosen. A sampling of various firms specializing in optical coatings also indicate that the nominal value of 0.5% represents the lowest reflectivity value to be expected over the range from 0.40 to 0.62 microns. These coatings will satisfy MIL-C-675 specifications for abrasive resistance and weathering characteristics.

V Mechanical Considerations

The cell will be made of a stainless steel which most nearly matches the glasses with regards to the thermal co-efficient of expansion. The elements will be edge shimmed at assembly for zero clearance. A window, for protection of the optical elements, is provided at the front of the cell and is removable by means of one

retaining ring.

The lens will incorporate a lockable focussing arrangement providing 2mm of motion on each side of best focus. The focus housing will engage the 2.118-48 thread and a shoulder will bottom on the system face. The lens cell is piloted in the focus housing on two lands and moves axially by means of a 12 pitch thread. Locking is accomplished by a set screw.

Light baffling will be accomplished by providing all retainers and spacers with deep grooves such that light entering the grooves cannot continue downstream except after two or more reflections. All retainers and spacers will be surface treated for minimum reflectivity with minimum specular component.

TABLE I

TABLE OF TOLERANCES

<u>SURFACE</u>	<u>ΔR</u>	<u>SURFACE FIGURE</u>	(ELEMENT CT) <u>Δd</u>	AIR SPACE <u>Δs</u>	<u>$\Delta N \bar{\lambda}$</u>	<u>WEDGE</u>	<u>ELEMENT TILT LENS SEAT</u>	<u>ELEMENT DECENTER</u>
1{2	± 0.014	.50 λ	± 0.0040	-	± 0.0016	0.0012"	0.0011"	0.0010"
3	± 0.012	.50 λ		± 0.0014				
2{4	± 0.003	.33 λ	± 0.0011		± 0.0008	0.0004"	0.0004"	0.0008"
5	± 0.015	.33 λ		± 0.0018				
3{6	± 0.004	.25 λ	± 0.0015		± 0.0011	0.0002"	0.0003"	0.0004"
7	± 0.001	.25 λ		± 0.0012				
-8	-			± 0.0012				
4{9	± 0.012	.25 λ	± 0.0014		± 0.0020	0.0004"	0.0002"	0.0006"
10	± 0.002	.25 λ		$\pm 0.0006^*$				
5{11	± 0.002	.25 λ	± 0.0017		± 0.0006	0.0002"	0.0003"	0.0004"
12	± 0.001	.33 λ		± 0.0031				
6{13	± 0.005	.50 λ	± 0.004		± 0.0016	0.0005"	0.0007"	0.0019"
14	± 0.246	.50 λ						

Note: All glasses must be Schlieren Grade, PH4 quality with Special Bubble Selector.

*MAY REQUIRE ASSEMBLY ADJUSTMENT

General Surface Finish:

	<u>Target</u>	<u>Required</u>
Element I and II	0/0	5/0
Elements III, IV, V VI	5/5	10/5

TABLE II

DISTORTION VALUES

FIELD ANGLE (Radius)	GAUSSIAN HEIGHT (mm)	IMAGE CENTROID (mm)	DISTORTION* (min)
0.000	0.0000	0.000	0.00
0.026105	1.3057	1.2992	0.44
0.05221	2.6141	2.6043	0.67
0.078315	3.9278	3.9128	1.02
0.104420	5.2497	5.2268	1.56
0.130525	6.5826	6.5558	1.83

Tolerance Value = 3.0 min.

TABLE III

TRANSMISSION & REFLECTION LOSSES: 400 NM

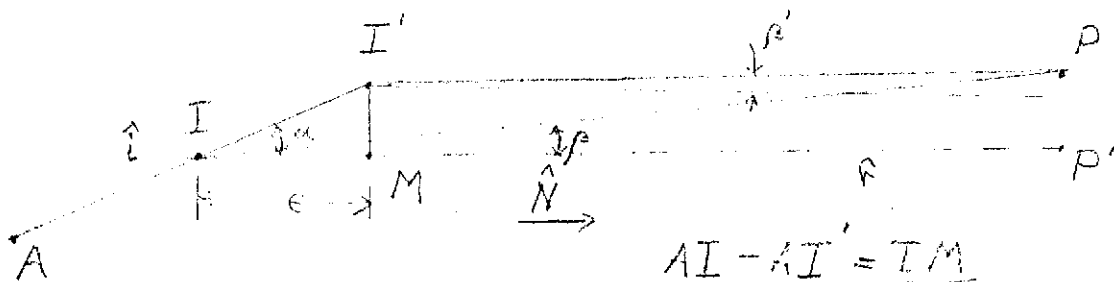
<u>MATERIAL</u>	<u>INTERNAL TRANSMITTANCE</u>	
	<u>5mm</u>	<u>25mm</u>
LAK-8	0.988	0.940
SF-19	0.985	0.920
SF-1	0.980	0.890

Reflection losses for 12 air-glass interfaces, assuming a very realistic coating value loss of 0.5%, will amount to 5.8%. The total absorption losses will be, nominally, less than 15.1%. Therefore, the average transmittance of the system will be about 79.1%. This value is somewhat pessimistic since the absorption values are given for plane parallel plates of glass and the lens elements are much thinner at the edges. The coatings will be broad band coatings, peaked for 4,000Å. The target value of 70% than appears to be definitely a practical working value.

APPENDICES

Appendix I. Calculation of Optical Path Errors Due to Surface Defects.

Consider first a refracting surface separating two media of indices n_1 and n_2 . If a defect of depth ϵ is present, the difference in optical path for the ray that is refracted at I and the ray that would have been refracted at I' if the defect were absent is, from the figure,



$$AI - AI' = \frac{IM}{\cos \alpha}$$

$$IP - I'P = \frac{I'P' - MP'}{\cos \beta'}$$

$$\Delta L = n_1 (AI - AI') + n_2 (IP - I'P) \quad (a.1)$$

Let $\Delta L = n_1 \left(\frac{IM}{\cos \alpha} \right) + n_2 \left(\frac{I'P'}{\cos \beta'} - \frac{MP'}{\cos \beta'} \right)$

then,

$$\vec{II'} = -\Delta \vec{I}$$

$$IM = \Delta \vec{I} \cdot \hat{N}$$

$$IP' = \vec{IP} \cdot \hat{N}$$

$$MP = \vec{I'P} \cdot \hat{N} \quad (a.2)$$

where \hat{N} is the unit normal to the surface in the absence of defects. Substituting Eqs. (a.2) into Eq. (a.1) leads to

$$\delta L = n_1 \left(\frac{\delta \vec{I} \cdot \hat{N}}{\cos \alpha} \right) + n_2 \left(\frac{\vec{I} \hat{P} \cdot \hat{N}}{\cos \beta} - \frac{\vec{I}' \hat{P} \cdot \hat{N}}{\cos \beta'} \right)$$

(a.3)

Since ϵ is assumed to be very small, $\beta = \beta'$ and

$$\vec{I} \hat{P} - \vec{I}' \hat{P} = - [\hat{P} \hat{I} - \hat{P} \hat{I}'] \delta \vec{I}$$

Hence,

$$\delta L = - (n_1 \hat{i} - n_2 \hat{i}') \cdot \delta \vec{I}$$

The law of refraction in vector form reads,

$$n_2 \hat{P} - n_1 \hat{i} = (n_2 \cos r - n_1 \cos i) \hat{N}$$

(a.4)

Therefore, we can write

$$\delta L = (n_2 \cos r - n_1 \cos i) \hat{N} \cdot \delta \vec{I}$$

But $\hat{N} \cdot \delta \vec{I} = \epsilon$. The deformation of the wave front is

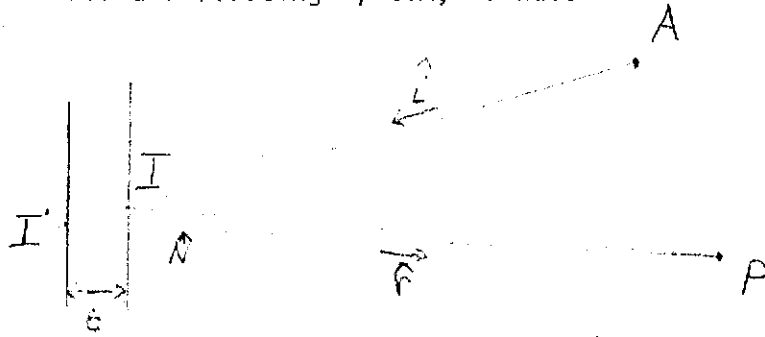
$$\Delta = -\delta L.$$

Consequently,

$$\Delta = (n_1 \cos i - n_2 \cos r) \epsilon$$

(a.5)

For a reflecting system, we have



$$\delta L = n [2\vec{i} \cdot \hat{N} + 2\vec{r} \cdot \hat{N}]$$

But the law of reflection in vector form reads

$$\hat{r} = -\hat{i} + 2 \cos i \hat{N}$$

Hence,

$$\delta L = n [2 \cos i \delta \vec{i} \cdot \hat{N}]$$

Again, $\hat{N} \cdot \vec{i} = \epsilon$ Hence, the deformation of the wave front is

$$\Delta = 2 n \epsilon \cos i$$

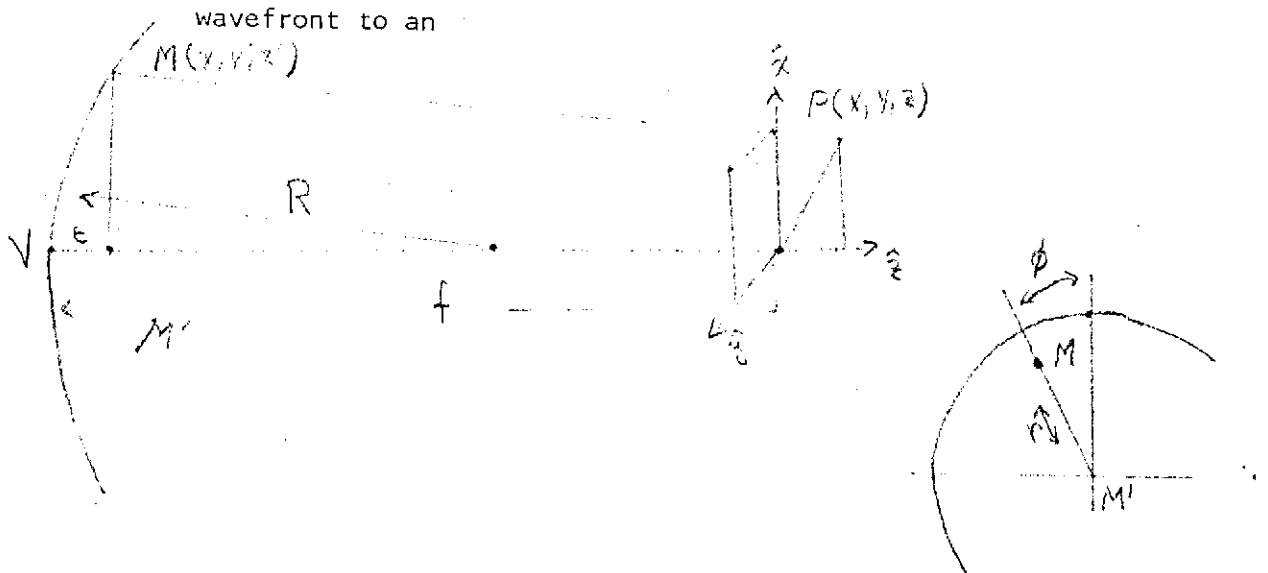
(a.6)

Appendix 2. Computation of the Distance That Appears in the Diffraction Integral.

If a converging wave front has phases represented by a phase function $F(x', y', z')$, the amplitude of the disturbance that reaches a point $P(x, y, z)$ is given by the classical Huygens-Fresnel formula (see, for example, ref. 6).

$$U(P) = -\frac{i}{\lambda} \iint F(x', y', z') \frac{e^{ikd_2}}{d_2} dS' \quad (b.1)$$

To evaluate d_2 , we consider an axially symmetric (or nearly so) wave front whose vertex is situated at a distance f from the origin of a coordinate system whose z -axis is in the direction of the symmetry axis. Let R represent the radius of curvature of the wave front at the vertex. From the figure it is clear that the distance from a point M on the wavefront to an



observation point near the plane x-y is

$$d_2^2 = (x-x')^2 + (y-y')^2 + (z-z')^2 \quad (b.2)$$

The position of the point M can be more conveniently specified by the coordinates r and ϕ plus the distance along the axis ϵ .

We can then write for d_2

$$d_2^2 = f^2 \left\{ 1 + \left(\frac{x}{f}\right)^2 + \frac{x^2 + y^2 + z^2}{f^2} - 2\left(\frac{\epsilon}{f}\right) + \left(\frac{\epsilon}{f}\right)^2 + 2\left(\frac{z}{f}\right)\left(1 - \frac{\epsilon}{f}\right) - 2\frac{x}{f} \left(\frac{x}{f} \cos \phi + \frac{y}{f} \sin \phi\right) \right\} \quad (b.3)$$

For the special but important cases where the wave front is spherical or paraboloidal, we have that

$$\epsilon^2 = R^2 \left[1 - \sqrt{1 - \left(\frac{x}{R}\right)^2} \right]^2$$

$$\epsilon = \frac{x^2}{2R}$$

and

respectively.

A simplification is obtained when all five of the conditions

$$\text{hold } \frac{x}{f} \ll 1, \quad \frac{y}{f} \ll 1; \quad \frac{x}{f}, \frac{y}{f} \text{ and } \frac{z}{f} \ll 1 \quad (b.4)$$

In this case

$$d_2 = f \left[1 - \frac{r}{f} + \frac{r^2}{f^2} \left(1 - \frac{r}{f} \right) - \frac{r}{f} \left(\frac{x}{f} \cos \phi + \frac{y}{f} \sin \phi \right) \right]$$

This is the usual form of d_2 for diffraction work. We shall be interested in a different form and also in the case where $z = 0$, that is, we want to have the observation point in a plane, that in general will be the focal plane of a lens or a mirror. Let us introduce the new variables.

$$\frac{r \sin \phi}{f} = \sin \beta, \quad \frac{r \cos \phi}{f} = \sin \alpha$$

As seen from the following figure, the angles α and β are in orthogonal planes and allow us to write d_2 in the form

$$d_2 = f \left\{ 1 - \frac{r}{f} (x \sin \alpha + y \sin \beta) \right\}$$

(b.5)

Since the condition $r/f \ll 1$ implies that the angles

α and β are small, we can replace the sines by the angles and have only the linear combination as the variable part of the exponent, in which case the integral becomes a Fourier integral, with exponential term

$$e^{ikz} e^{-ik(x \cos \theta + y \sin \theta)}$$

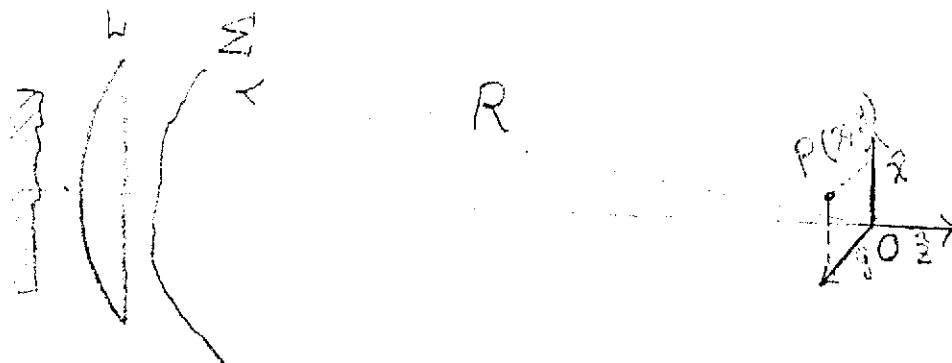
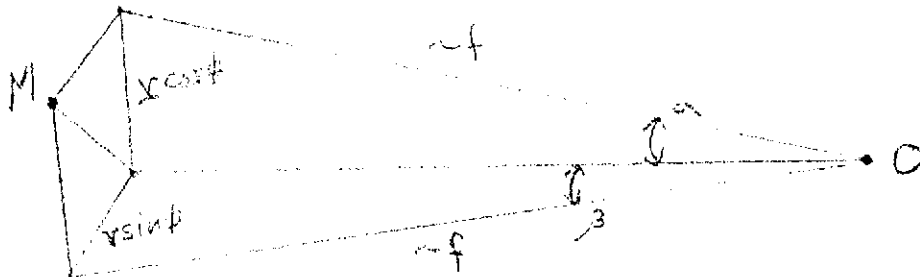


Figure 1

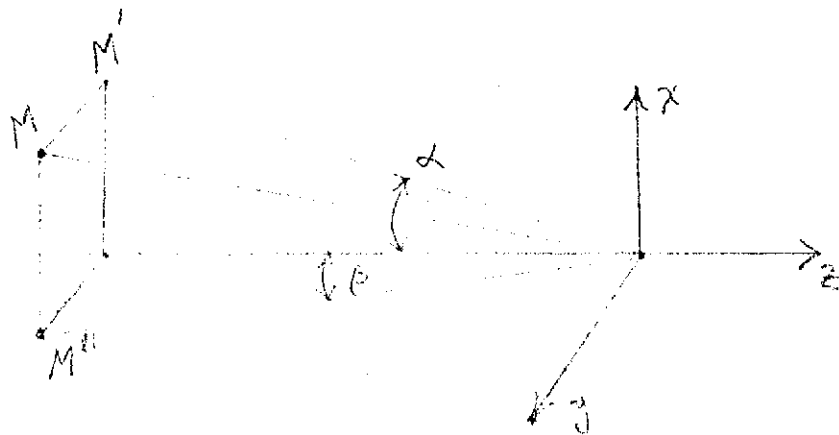


Figure 2

REFERENCES

1. J. Urbanek, Rev. d'Opt., p. 247 (1930)
2. A. Marechal, Opt. Acta, vol. 5, 70 - 74 (1958)
3. Diffieux, P. M., L'integrale de Fourier et ses applications a l'optique, Oberthur, Rennes (1946)
4. E. Diederichs, and A. Lohmann, Optik, vol. 12, 751 (1958)
5. Linfoot, E. H., Fourier methods in Optical image evaluation, The Focal Press, New York (1964)
6. Born, M. and Wolf, E., Principles of Optics, New York, (1964)
7. Goodman, J. W., Introduction to Fourier Optics, New York, (1968)
8. G. Kuwabara, J. Opt. Soc. Am., vol. 43, No. 1 (1953)

Appendix 3. Sample Scattering Computation.

Computations are based on the following three equations that represent the amount of light scattered by an irregularity as a fraction of the flux incident on it.

For Bubbles:

$$\epsilon = 16\pi \left\{ \frac{\lambda (n-1)}{R_o} \right\}^2 \left(\frac{\omega}{\lambda} \right)^6 f_1(\theta) f_2(d)$$

For scratches:

$$\epsilon = (2\pi)^3 (n-1)^2 \left(\frac{h}{\lambda} \right)^2 \frac{\Delta x \Delta y}{R_o^2} f_1(\theta) f_1(d)$$

For bulk inhomogeneities:

$$\epsilon = \left(\frac{2\pi t}{\lambda} \right)^2 \left(\frac{\Delta n}{N} \right)^2 f_1(\theta) f_1(d)$$

where

- λ = wave length of light
- n = index of refraction of glass
- R_o = radius of curvature of wave front forming image
- ω = radius of bubble
- $\Delta x, \Delta y$ = dimension of scratch determining projected area
- h = depth of scratch
- t = thickness of lens or optical element
- Δn = fluctuation of index in optical element
- N = av. number of domains/unit thickness showing the fluctuation Δn .
- $f_1(\theta)$ = factor to account for angular distribution of scattered light
- $f_2(d)$ = factor to account for defocussing effects that tend to spread out the light over the image pane.

For bubbles, for example, we have selected a glass belonging to bubble group 0, specified as having a total bubble cross section between 0 and $0.029 \text{ mm}^2/100\text{cc}$ volume of glass. We shall assume a value of 0.010, for 1st element. For the 6-element system, we further require that there be no bubble or inclusion of diameter 50μ or greater. This is consistent with the lower limit of bubble group 0. Since the 1st element of the system has an approximate volume of 30cc, we have a total area, according to specifications, between 0 and $0.01 (\text{mm})^2$. Assuming a log-normal distribution for the bubble present, the mean bubble radius is in the vicinity of 20λ . The radius of curvature of the front surface will be taken as 10cm and for a 20λ bubble with direct illumination from a direction making an angle of 30° with the optic axis we have an angular factor $\leq 10^{-3}$. With these values, and recalling that the true image plane is about 2.5 cm behind the last element we have

$$\begin{aligned}
 \epsilon &= 16\pi \left\{ \frac{.16 \times 10^{-8}}{4 \times 100} \right\} \frac{(10)^6}{.4 \sqrt{\pi}} \times 10^{-3} \\
 &= 16\pi \left(\frac{16 \times 10^{-10}}{4 \times 10^2} \right) \frac{(10^{12})}{4^6 \times \pi^3} \times 10^{-3} \\
 &= \frac{10^{-4}}{64} \approx 1.6 \times 10^{-6}
 \end{aligned}$$

For this case, we have taken $f_2(d)=1$, to consider what might be regarded as a worse case. For scratches, we have taken the angular factor to be 1, since there may be cases where the orientation of a very narrow scratch spreads the light over a considerable angle from the direction of the incident light.

For bulk inhomogeneities, we consider an element 14mm thick made of glass in homogeneity group H² ($\Delta n = \pm 5 \times 10^{-6}$). Since N is of order $(10^4)^{-1} \text{ cm}^{-1}$, we have

$$\begin{aligned} \epsilon &= (5 \times 10^{-6})^2 \frac{(2\pi \times 1.4)^2}{4 \times 10^{-5}} \frac{10^{-3}}{1.4 \times 10^3 \times 2.5} \\ &= 1/3 \times 10^{-6} \end{aligned}$$

We also have assumed that when illumination is such that more than one element receives light from the source, the net effect is additive.

Appendix 4. Computer Design Data.



E.P. LOCATION

1-10	0.00000000	+40000000		
1-0	-2.69992512	1.00000000	0.00000000	.02706479
2-3 R	3.59887889	-0.00000000		
2-1 L	.54735222	1.72135300	54.69410000	.00332940
3-3 R	-6.10936901	-0.00000000		
3-1 L	.00409174	1.00000000	0.00000000	.02706479
4-3	7.84401385	-0.00000000		
4-1	.63253628	1.72135300	54.69410000	.00332940
5-3	4.25087782	-0.00000000		
5-1	.15607832	1.00000000	0.00000000	.02706479
6-3	-2.86141478	-0.00000000		
6-1	.25083480	1.67971500	32.23500000	.09636757
7-3	.99928437	-0.00000000		
7-1	.17926524	1.00000000	0.00000000	.02706479
8-3	0.00000000	-0.00000000		
8-1	.06979460	1.00000000	0.00000000	.02706479
9-3	-2.6013362	-0.00000000		
9-1	.20010314	1.73293700	28.65500000	.09939056
10-3	7.99530907	-0.00000000		
10-1	.00241218	1.00000000	0.00000000	.02706479
11-3	7.81060819	-0.00000000		
11-1	.64039832	1.72135300	54.69410000	.00332940
12-3	-7.23557581	-0.00000000		
12-1	.08399380	1.00000000	0.00000000	.02706479
13-3	7.50874608	-0.00000000		
13-1	.38039748	1.72135300	54.69410000	.00332940
14-3	27.84930678	-0.00000000		
14-1	7.00716463	1.00000000	0.00000000	.02706479
15-3	0.00000000	-0.00000000		
15-2	-.00346960	1.00000000	0.00000000	.02706479
16-3	0.00000000	0.00000000		
16-1	0.00000000	1.00000000	0.00000000	0.00000000

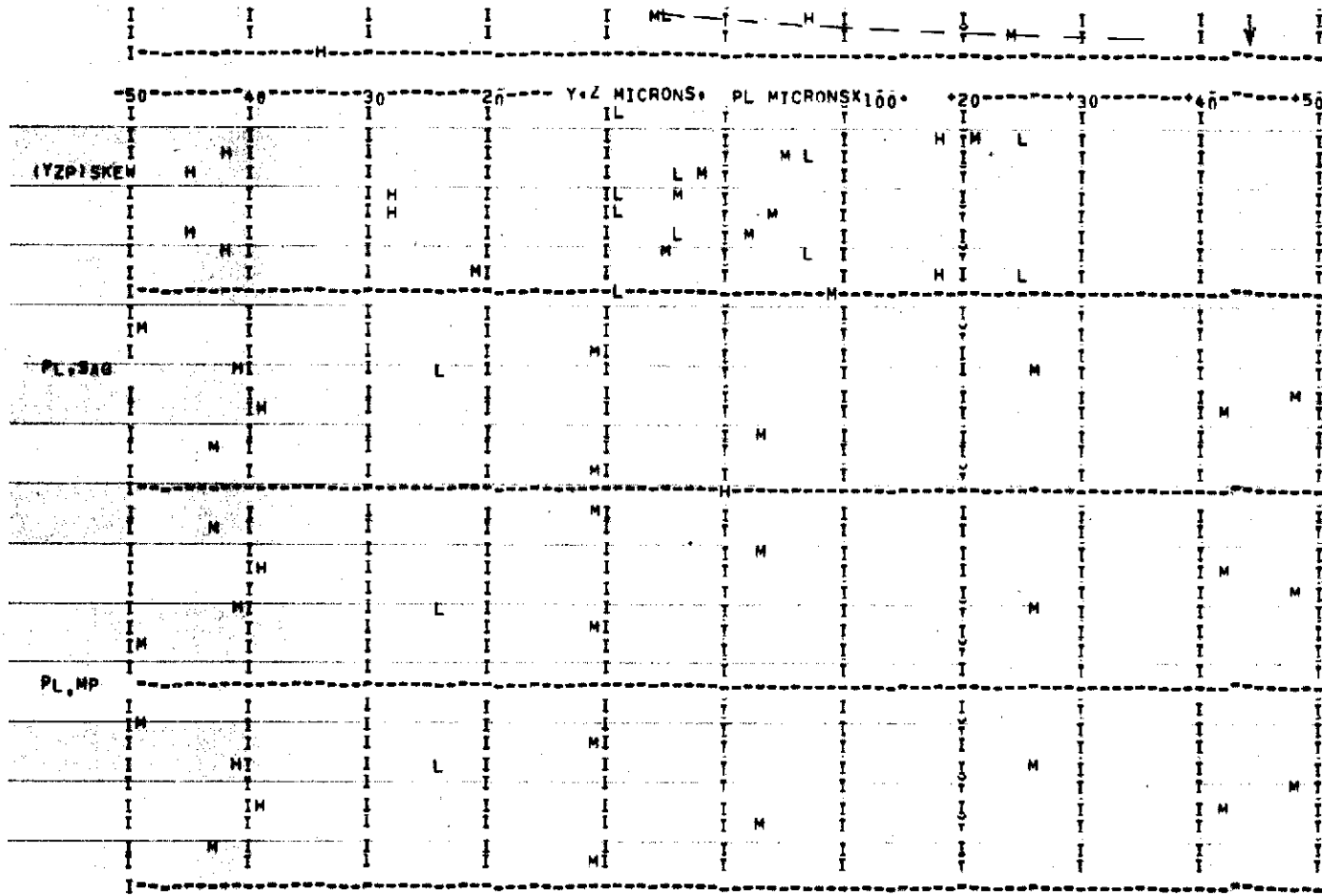
50 MM F/1.03 LOW SCATTER LENS SYSTEM

CONSTRUCTION DATA

RAY HEIGHT VS INTERCEPT ERRORS

64

Page 64



66

Page 66

R/CT ↓

Nλ (0.4 - 0.6 μ)

LOW SCATTER 50 MM F/1.

SYSTEM DATA (MM)

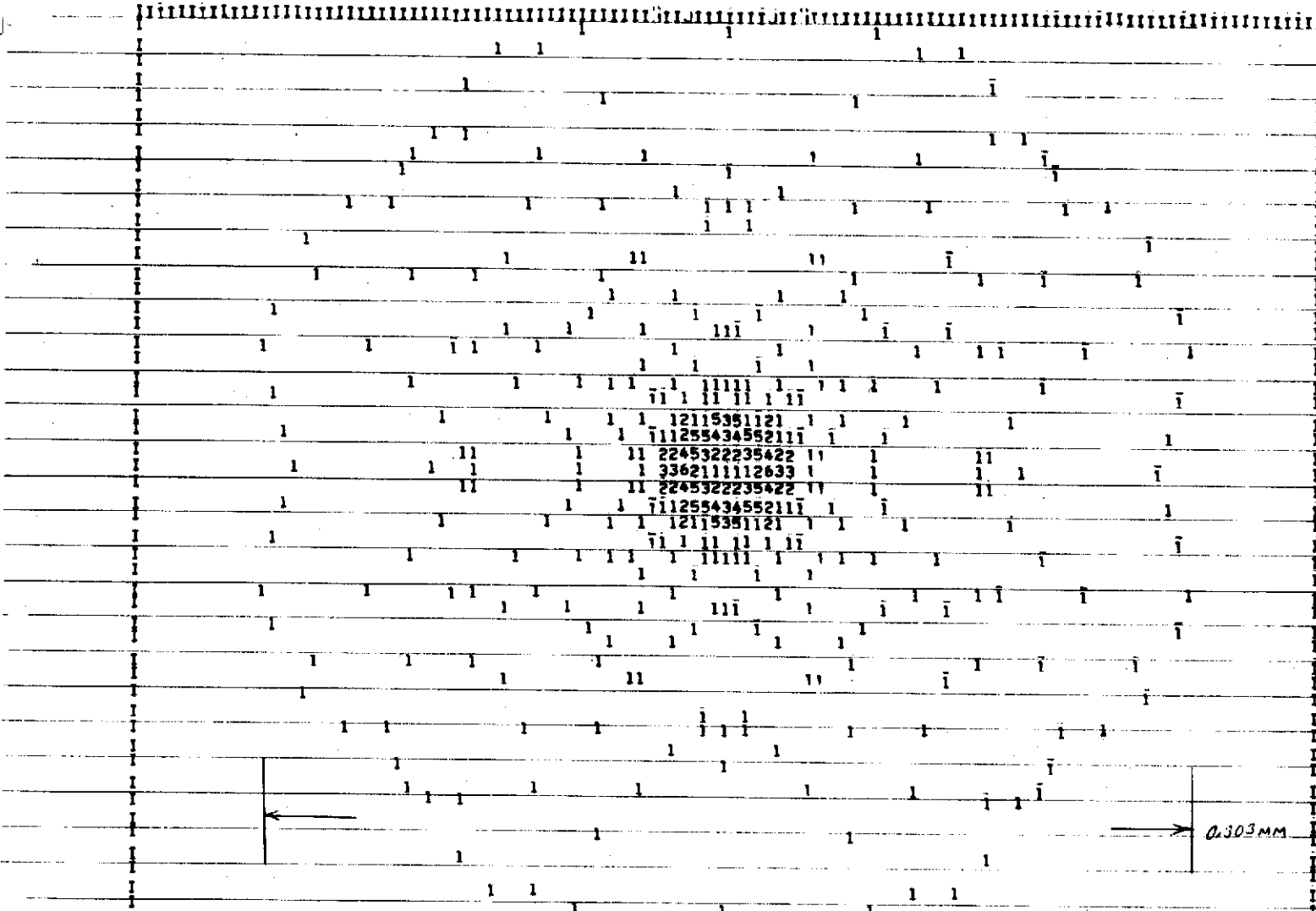
2	89.071472	-0.	-0.	-0.	-0.	-0.	-0.	-0.	-0.
2	13.4048805	1.736479	1.727143	1.723612	1.720619	1.718053	1.715831	1.712177	
3	-152.734225	-0.	-0.	-0.	-0.	-0.	-0.	-0.	
3	1.02204	1.000000	1.000000	1.000000	1.000000	1.000000	1.000000	1.000000	
4	46.100346	-0.	-0.	-0.	-0.	-0.	-0.	-0.	
4	15.013407	1.736479	1.727143	1.723612	1.720619	1.718053	1.715831	1.712177	
5	106.571938	-0.	-0.	-0.	-0.	-0.	-0.	-0.	
5	3.001958	1.000000	1.000000	1.000000	1.000000	1.000000	1.000000	1.000000	
6	-51.535370	-0.	-0.	-0.	-0.	-0.	-0.	-0.	
6	6.350957	1.705295	1.689163	1.683353	1.678546	1.674509	1.671078	1.665571	
7	24.082109	-0.	-0.	-0.	-0.	-0.	-0.	-0.	
7	4.481031	1.000000	1.000000	1.000000	1.000000	1.000000	1.000000	1.000000	
8	0.000000	-0.	-0.	-0.	-0.	-0.	-0.	-0.	
8	1.744065	1.000000	1.000000	1.000000	1.000000	1.000000	1.000000	1.000000	
9	-67.503341	-0.	-0.	-0.	-0.	-0.	-0.	-0.	
9	1.322022	1.764271	1.744437	1.737355	1.731519	1.726637	1.722500	1.715888	
10	0.000000	0.	0.	0.	0.	0.	0.	0.	
10	3.680956	1.764271	1.744437	1.737355	1.731519	1.726637	1.722500	1.715888	
11	49.882727	-0.	-0.	-0.	-0.	-0.	-0.	-0.	
11	1.060304	1.000000	1.000000	1.000000	1.000000	1.000000	1.000000	1.000000	
12	45.265205	-0.	-0.	-0.	-0.	-0.	-0.	-0.	
12	16.009458	1.736479	1.727143	1.723612	1.720619	1.718053	1.715831	1.712177	
13	-30.889383	-0.	-0.	-0.	-0.	-0.	-0.	-0.	
13	1.99845	1.000000	1.000000	1.000000	1.000000	1.000000	1.000000	1.000000	
14	37.718652	-0.	-0.	-0.	-0.	-0.	-0.	-0.	
14	9.509437	1.736479	1.727143	1.723612	1.720619	1.718053	1.715831	1.712177	
15	546.232520	-0.	-0.	-0.	-0.	-0.	-0.	-0.	
15	25.179116	1.000000	1.000000	1.000000	1.000000	1.000000	1.000000	1.000000	
16	0.000000	-0.	-7.970000E-05	-2.640900E-04	-0.	9.981253E-01	1.000000	1.000000	
16	-0.086140	1.000000	1.000000	1.000000	1.000000	1.000000	1.000000	1.000000	

71

SPOT DIAGRAM ANALYSES

Page 71

X X# .034630



72

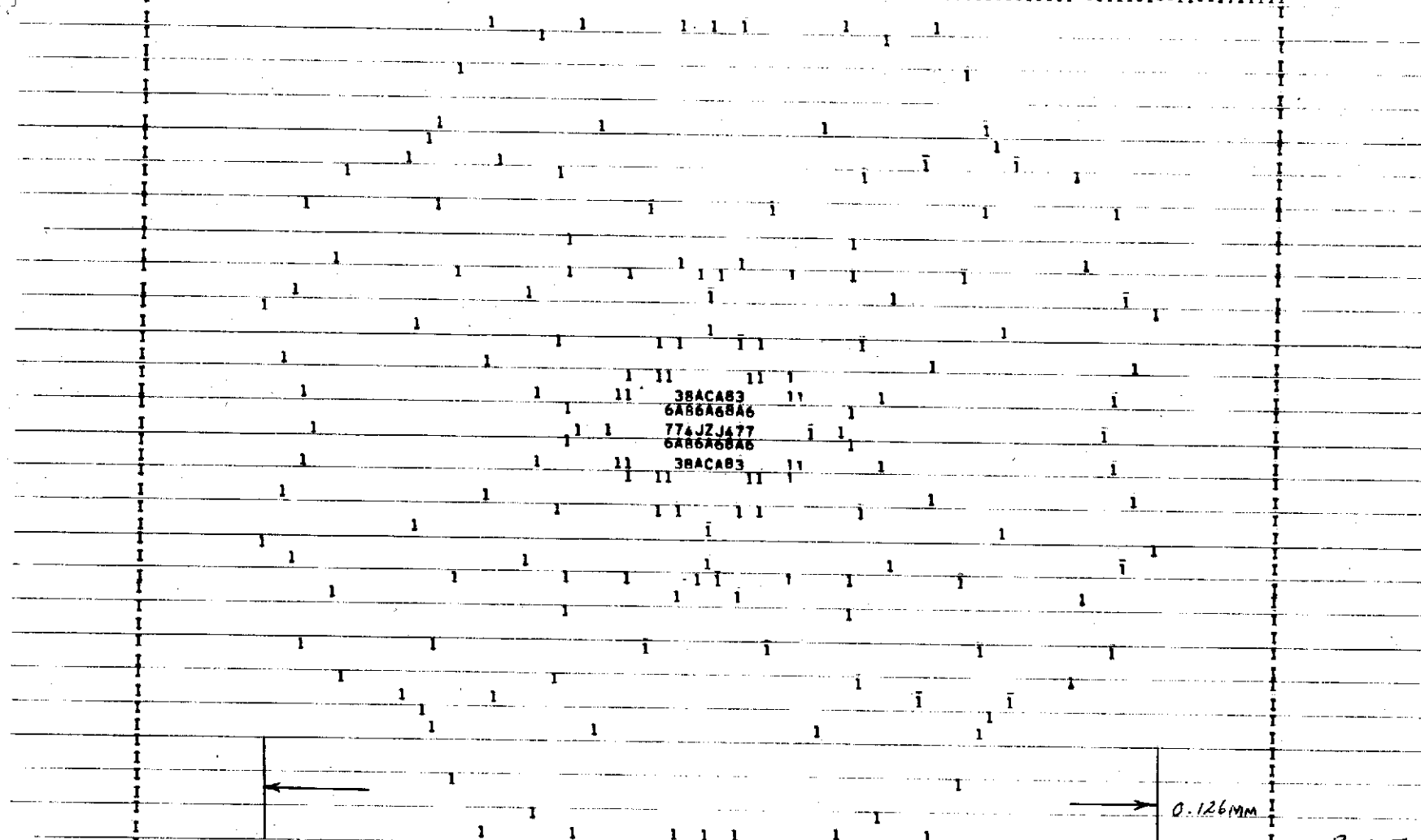
PAGE I

WAVELENGTH = .40000 IMAGE HEIGHT = .00000
 FIELD 1 4 RAYS OUTSIDE 184 RAYS BLOCKED OUT OF A TOTAL OF 729 RAYS

Page 72

X X= .014444

GL



3BAC83
 6AB668A6
 774JZJ477
 6AB668A6
 3BAC83

0.126mm

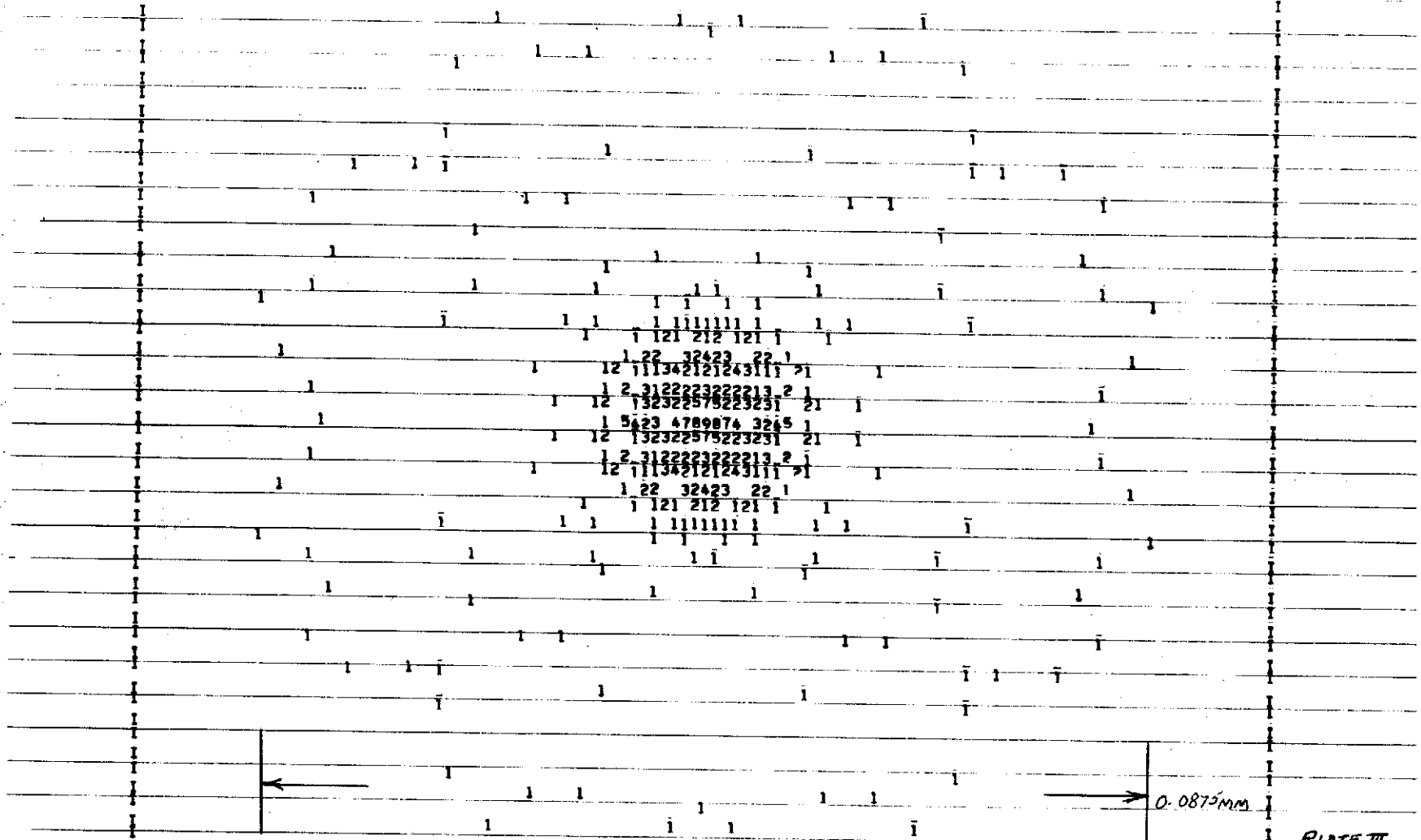
PLATE II

WAVELENGTH = 4500 IMAGE HEIGHT = .000
 FIELD 1 4 RAYS OUTSIDE 184 RAYS BLOCKED OUT OF A TOTAL OF 729 RAYS

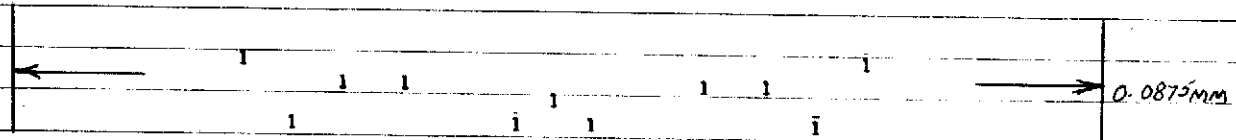
Page 73

X X* .010000

74



1 22 32423 22 1
 12 111342121243111 >1
 1 2 312222322213 2 1
 12 132322579223231 21
 1 523 4789874 3245 1
 12 132322579223231 21
 1 2 312222322213 2 1
 12 111342121243111 >1
 1 22 32423 22 1
 1 121 212 121 1

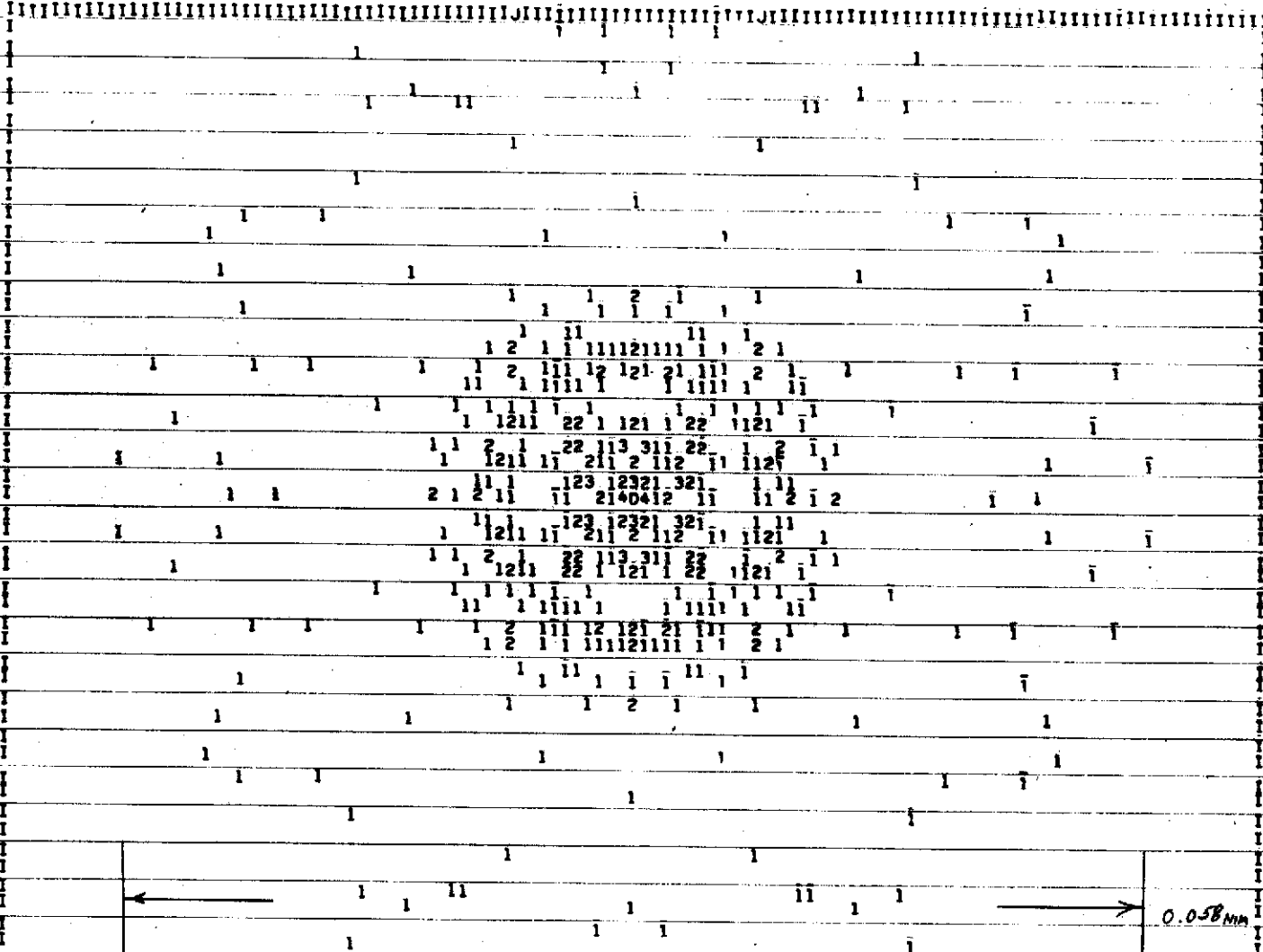


WAVELENGTH = 647500 IMAGE HEIGHT = .0000
 FIELD 1 4 RAYS OUTSIDE 184 RAYS BLOCKED OUT OF A TOTAL OF 729 RAYS

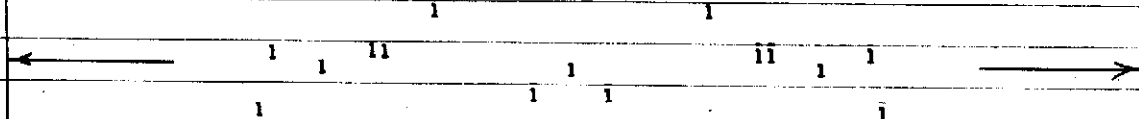
PLATE III

PLATE III

X X= .006481



76



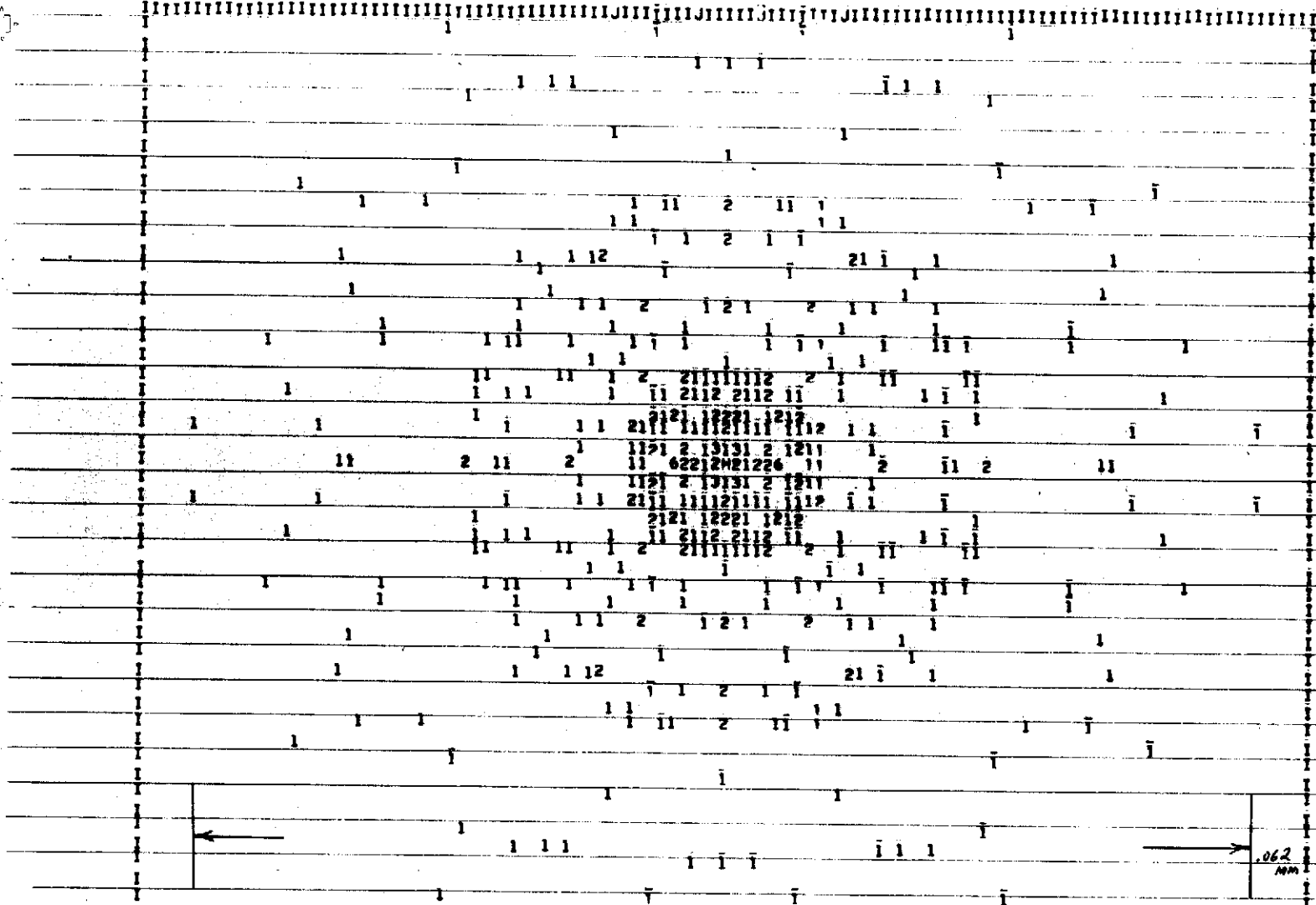
0.058mm

PART V

WAVELENGTH= .52500 IMAGE HEIGHT= 0000
 FIELD 1 0 RAYS OUTSIDE 184 RAYS BLOCKED OUT OF A TOTAL OF 729 RAYS

Page 76

X x= .006111



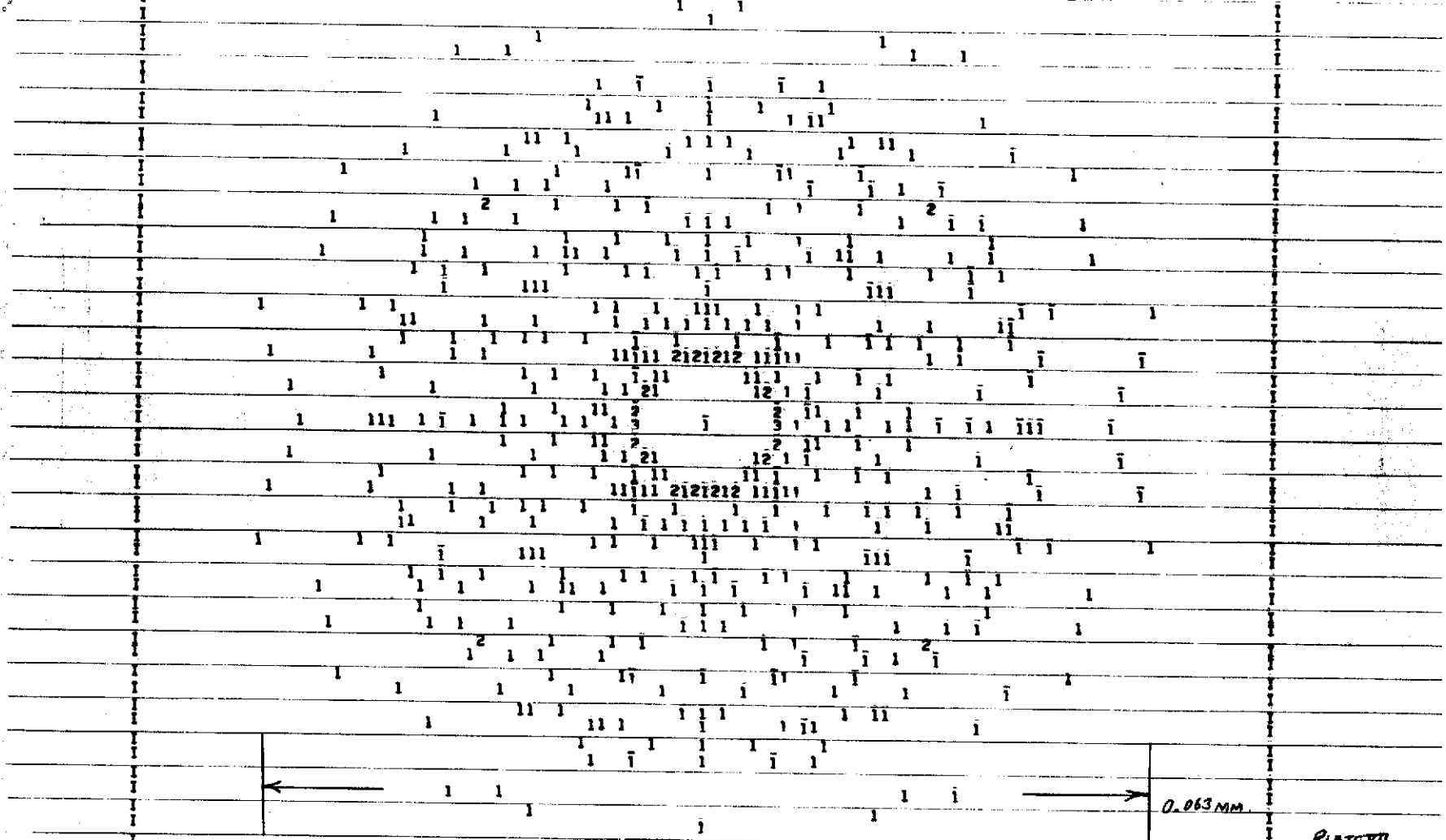
WAVELENGTHS 55000 IMAGE HEIGHTS .0000
 FIELD 1 0 RAYS OUTSIDE 184 RAYS BLOCKED OUT OF A TOTAL OF 729 RAYS

PLATE VI

Page 11

77

X= 007222



BL

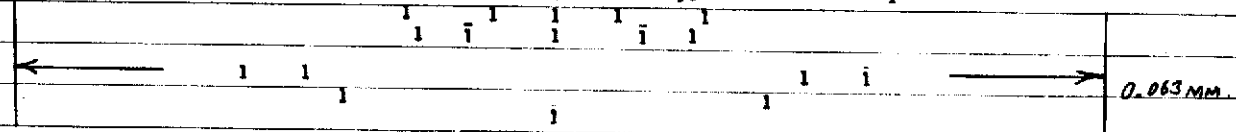


PLATE VII

WAVELENGTH = .60000 IMAGE HEIGHT = .0000
 FIELD 1 0 RAYS OUTSIDE 188 RAYS BLOCKED OUT OF A TOTAL OF 729 RAYS

Page 78

bl

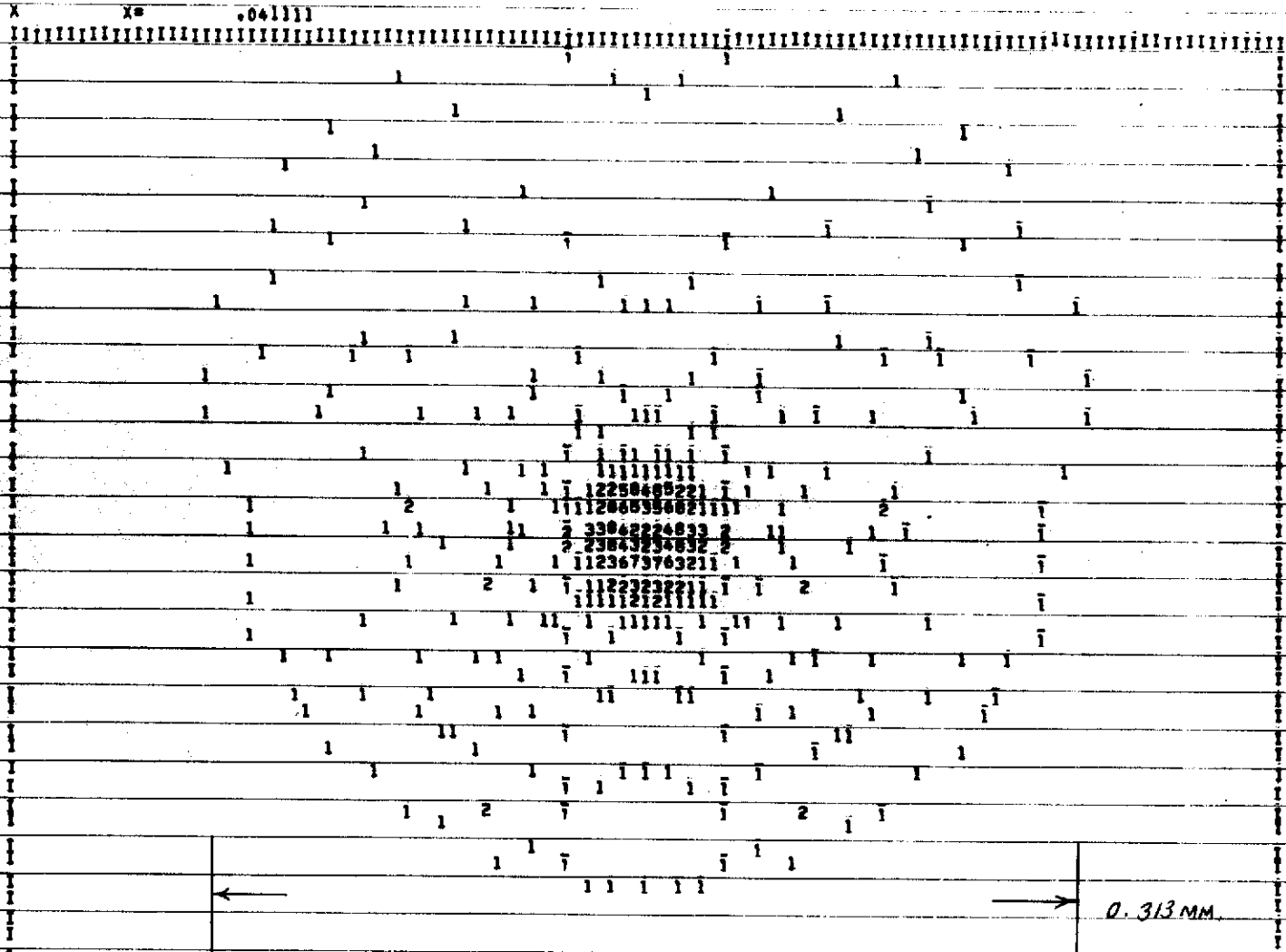
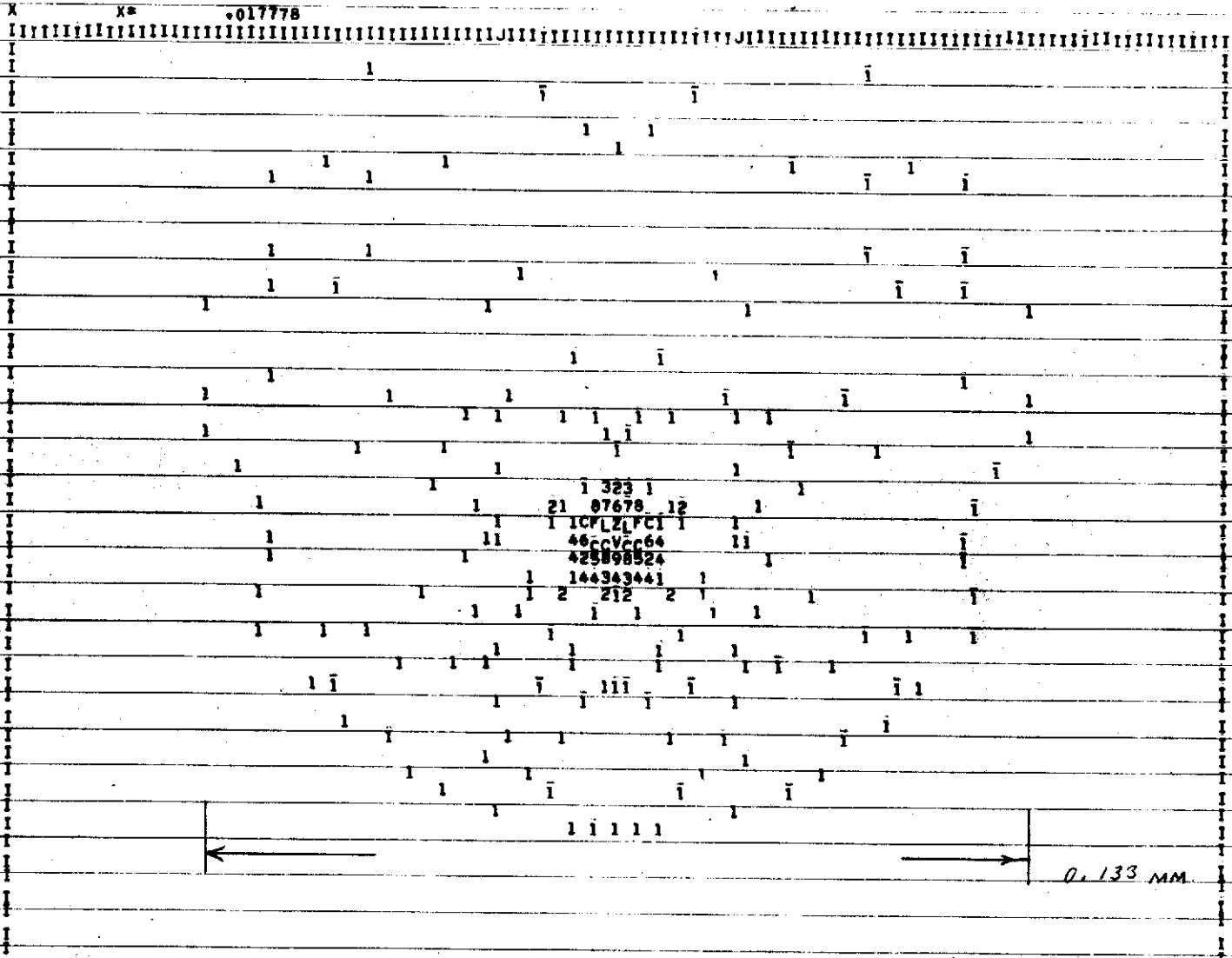


PLATE VII

WAVELENGTH 40000 IMAGE HEIGHT 1.2992

FIELD 2 4 RAYS OUTSIDE 200 RAYS BLOCKED OUT OF A TOTAL OF 729 RAYS

Page 79

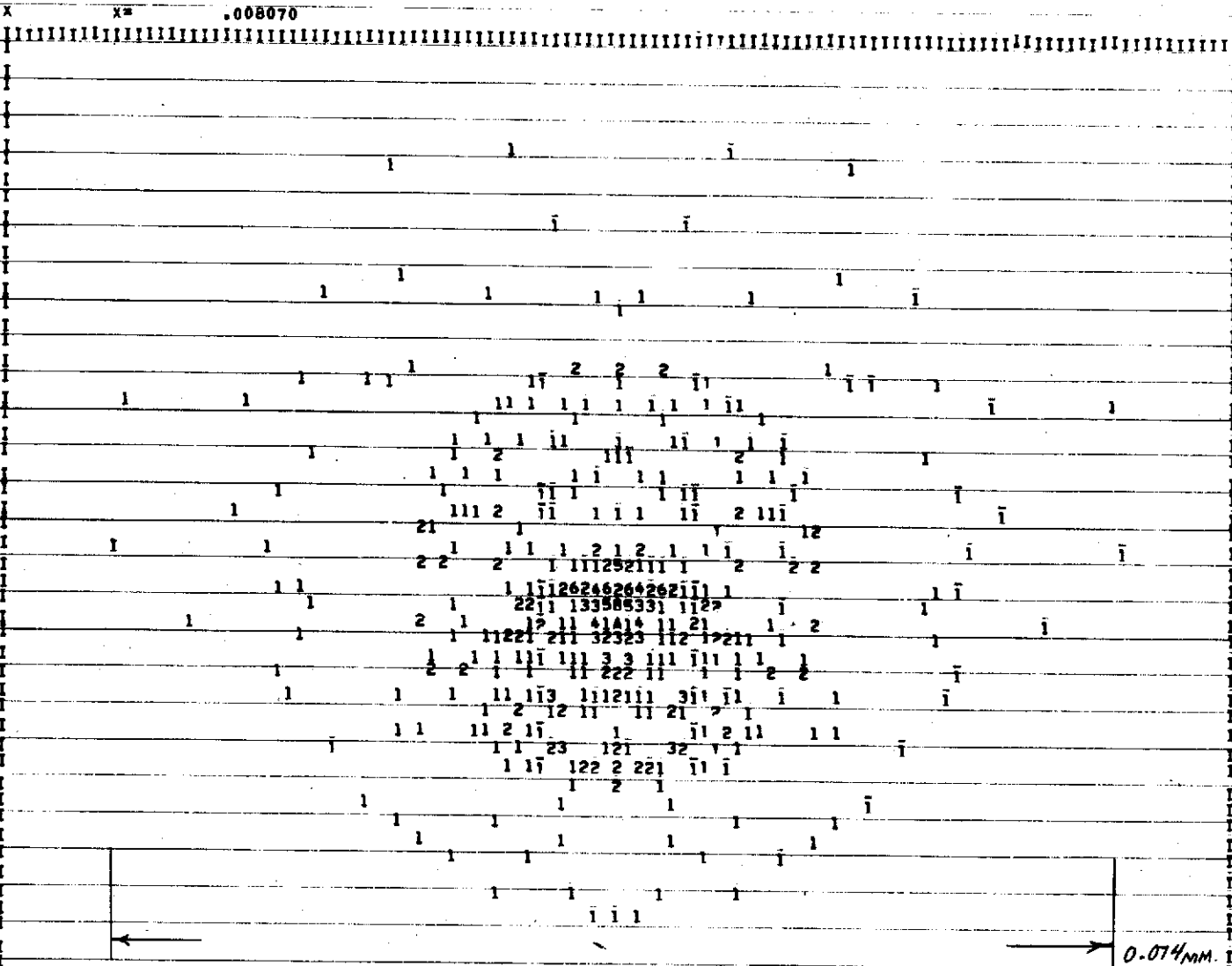


05

WAVELENGTH* 4500 IMAGE HEIGHT* 1.292
 FIELD 2 2 RAYS OUTSIDE 202 RAYS BLOCKED, OUT OF A TOTAL OF 729 RAYS

Page 86

x = .008070

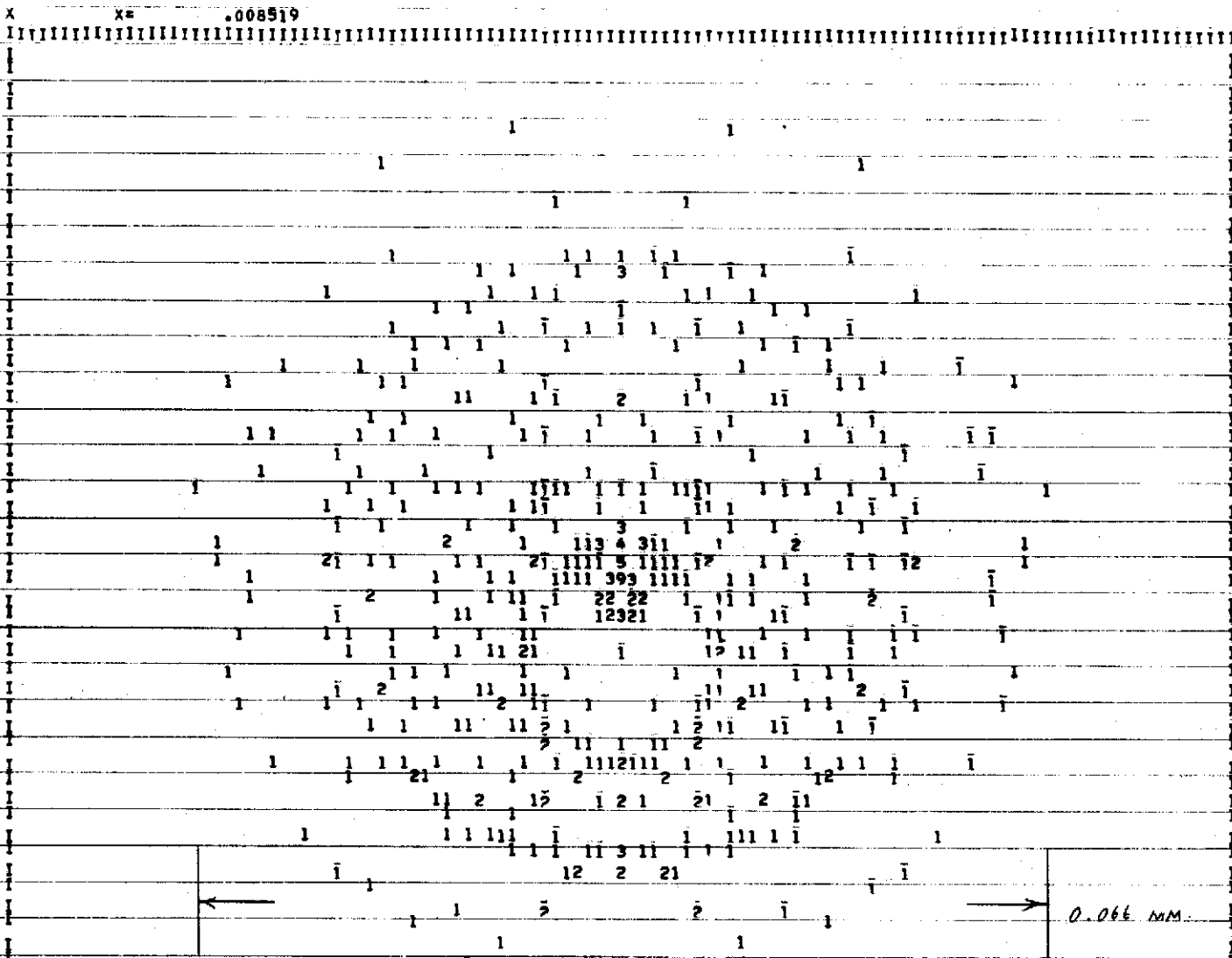


PAGE XII

WAVELENGTH 55000 IMAGE HEIGHT 1.2992
 FIELD 2 2 RAYS OUTSIDE 206 RAYS BLOCKED OUT OF A TOTAL OF 729 RAYS

84

Page 84



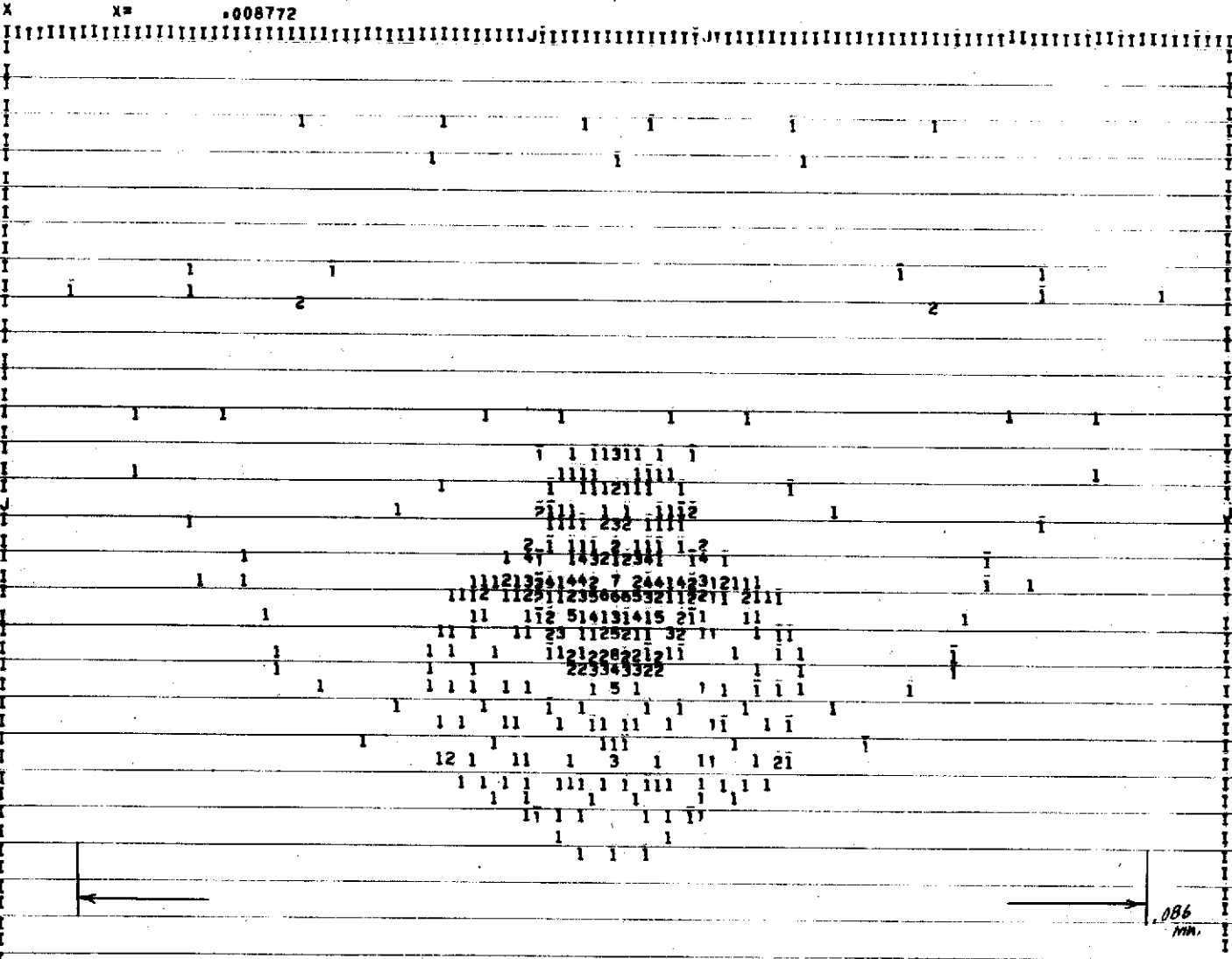
85

PLATE XIII

0.066 MM

WAVELENGTH = .60000 IMAGE HEIGHT = 1.2992
 FIELD 2 0 RAYS OUTSIDE 212 RAYS BLOCKED OUT OF A TOTAL OF 729 RAYS

Plate 85

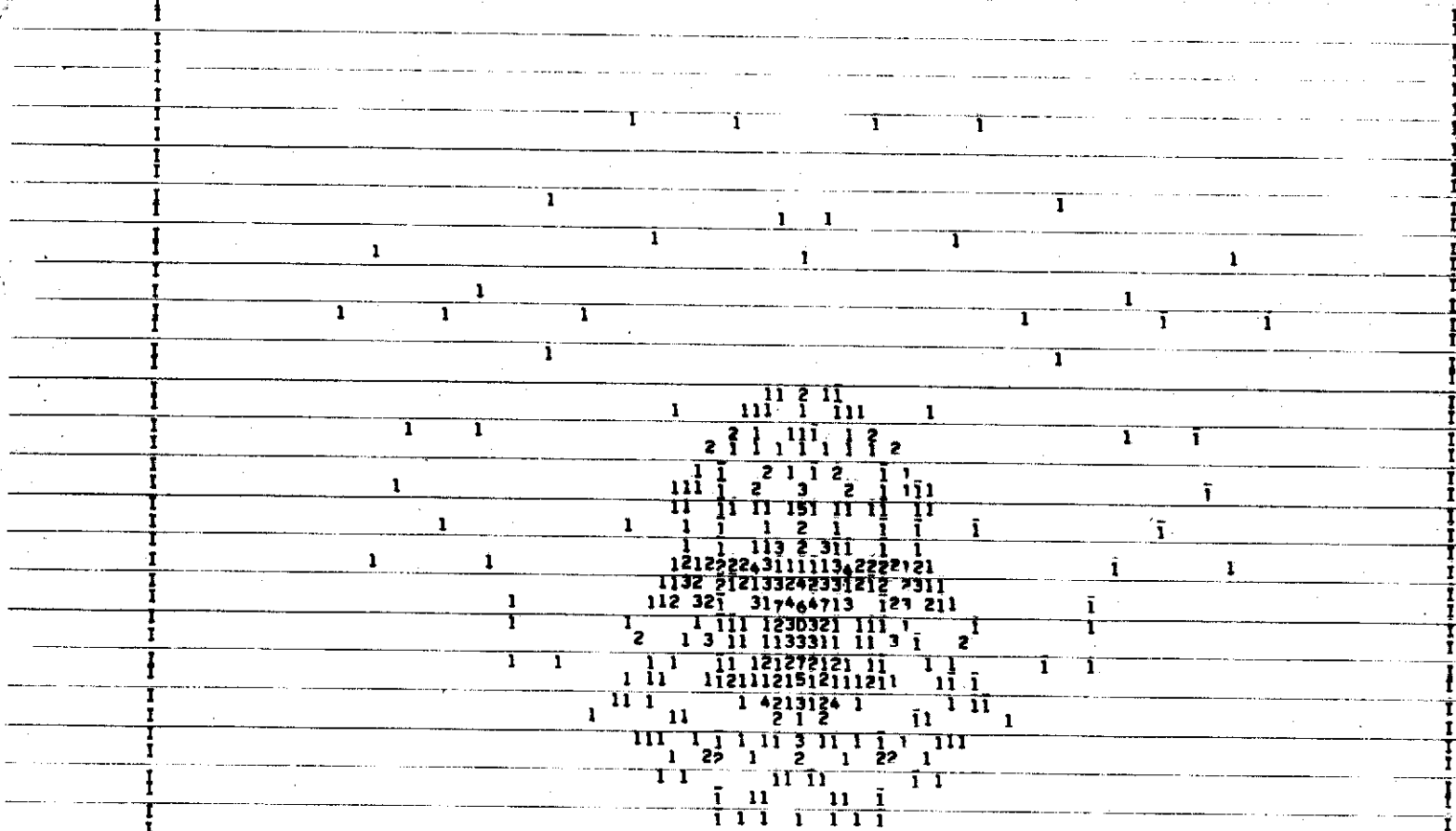


WAVELENGTH# .50000 IMAGE HEIGHT# 2.60*3
 FIELD 3 0 RAYS OUTSIDE 220 RAYS BLOCKED OUT OF A TOTAL OF 729 RAYS

Page 89

68

X 1009298



0.072 mm.

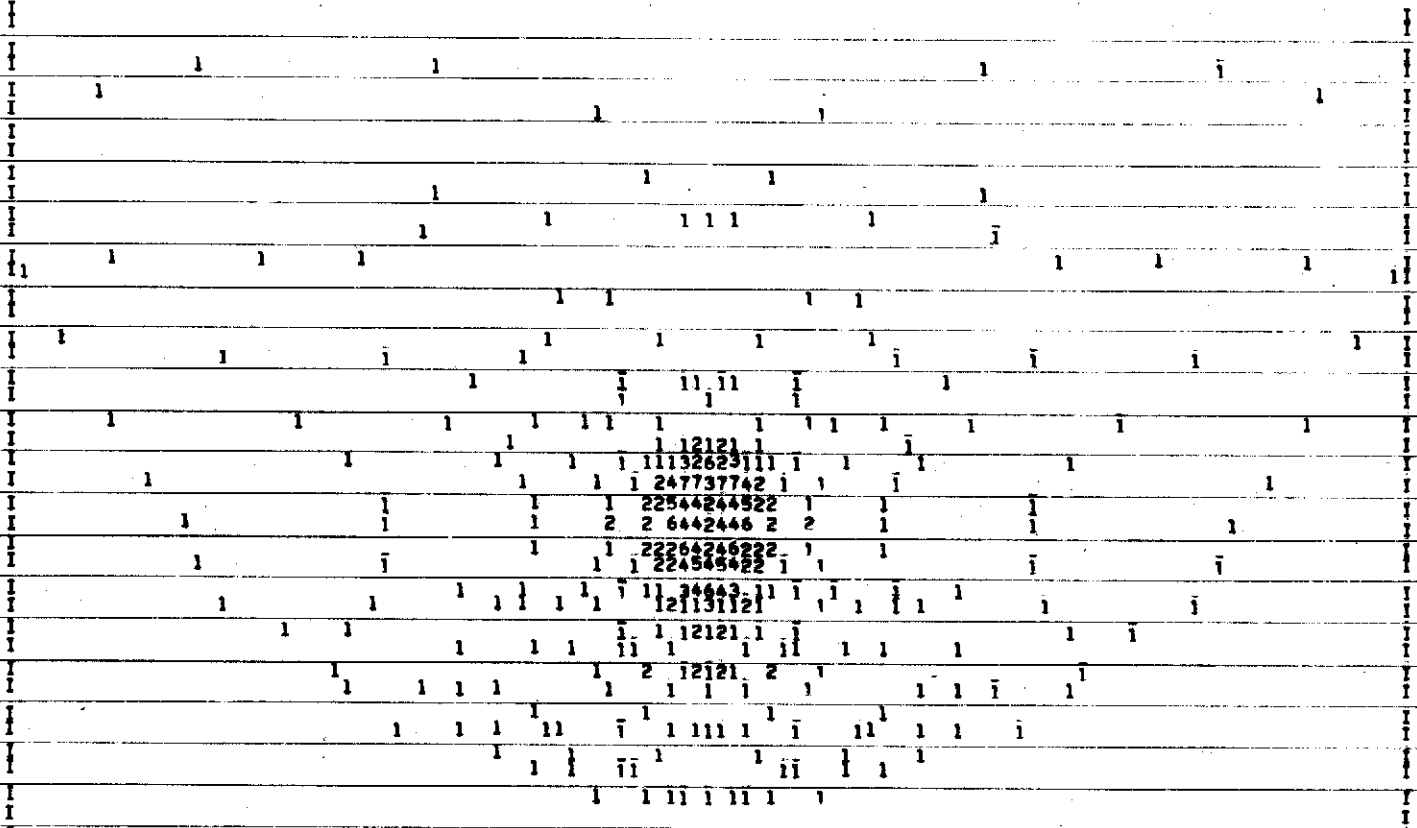
PLATE XVIII

WAVELENGTH = 5250 Å IMAGE HEIGHT = 2480 μ
 FIELD 3 2 RAYS OUTSIDE 222 RAYS BLOCKED, OUT OF A TOTAL OF 729 RAYS

Page 10

Ob

X X=.033158



93

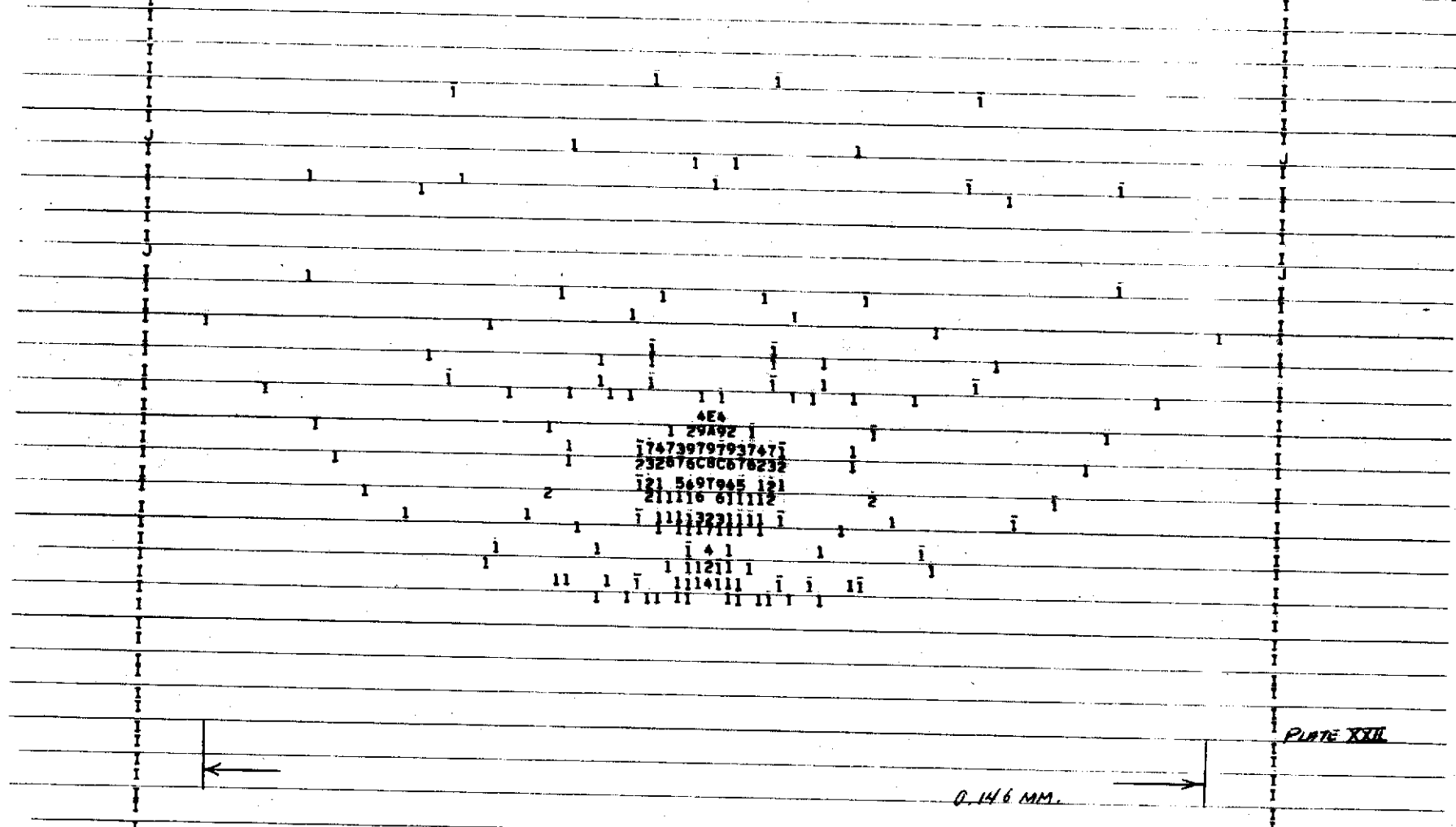
Part XXI



WAVELENGTH = .40000 IMAGE HEIGHT = 3.8128
 FIELD # 4 2 RAYS OUTSIDE 245 RAYS BLOCKED OUT OF A TOTAL OF 729 RAYS

Page 93

X= .014815



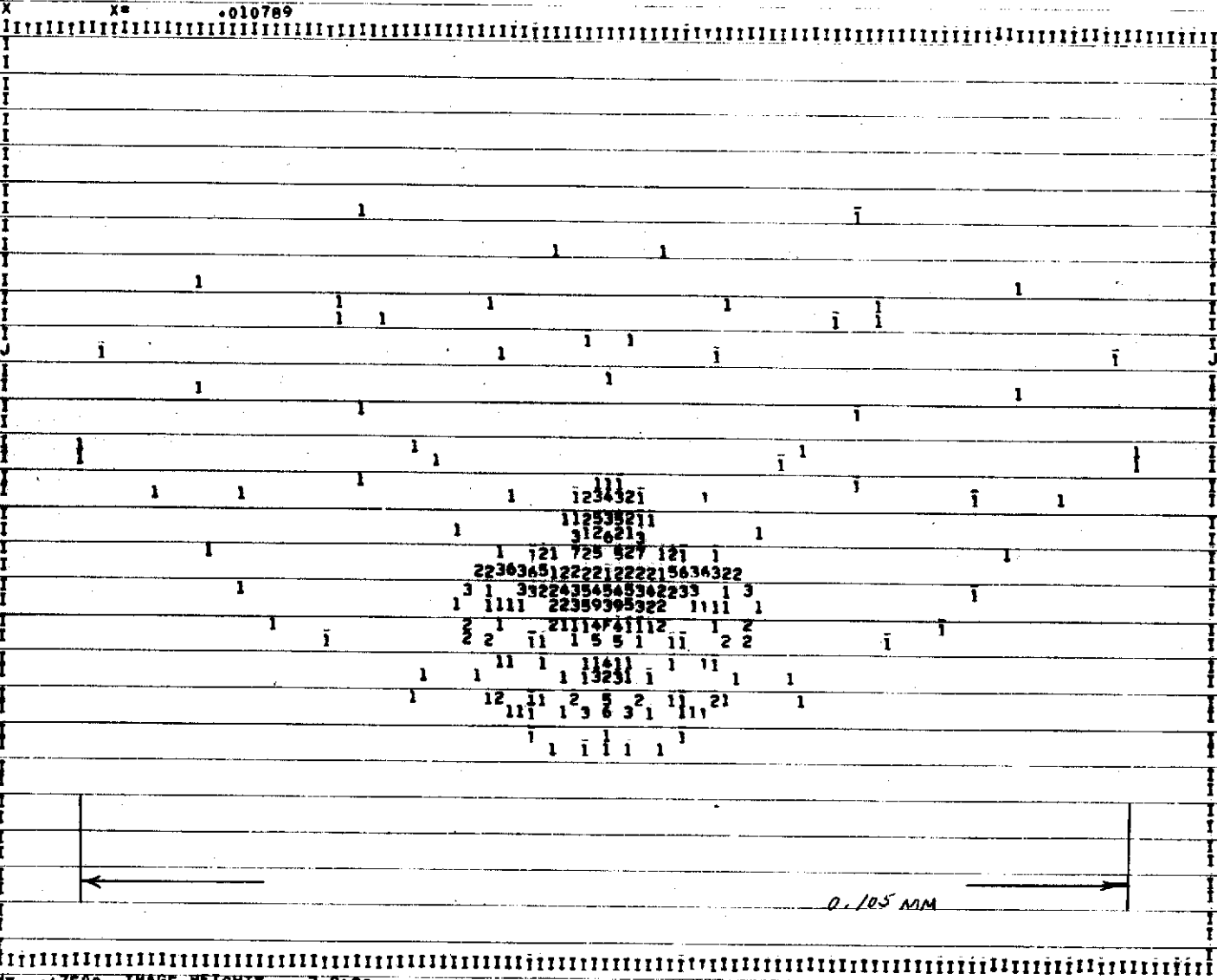
hb



PLATE XIII

WAVELENGTH= 45000 IMAGE HEIGHT= 39128
 FIELD 4 2 RAYS OUTSIDE 243 RAYS BLOCKED OUT OF A TOTAL OF 729 RAYS

Page 94



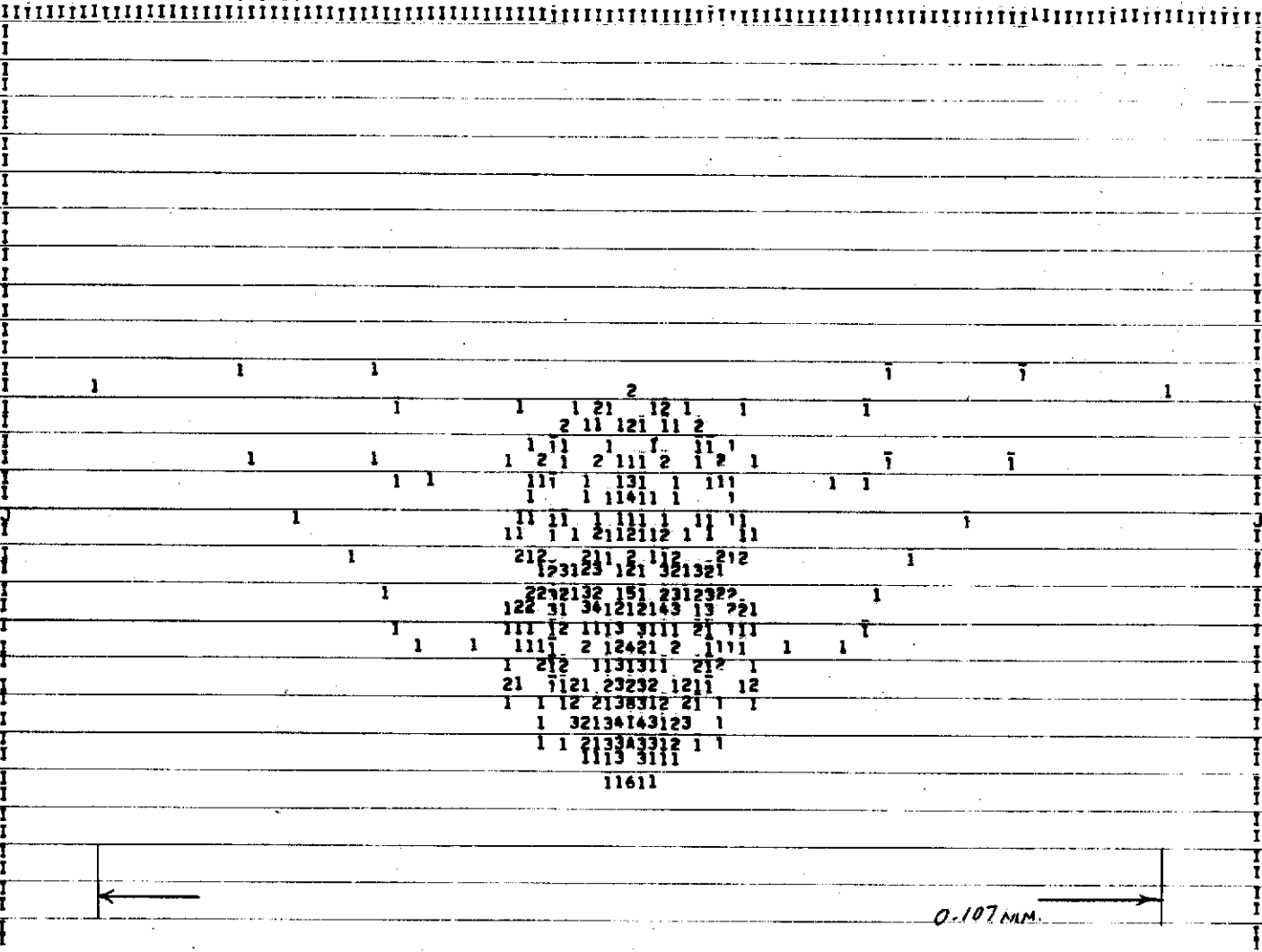
WAVELENGTH= .47500 IMAGE HEIGHT= 3.9128
 FIELD 4 2 RAYS OUTSIDE 243 RAYS BLOCKED OUT OF A TOTAL OF 729 RAYS

PLATE XXIII

Page 95

95

X* .011228



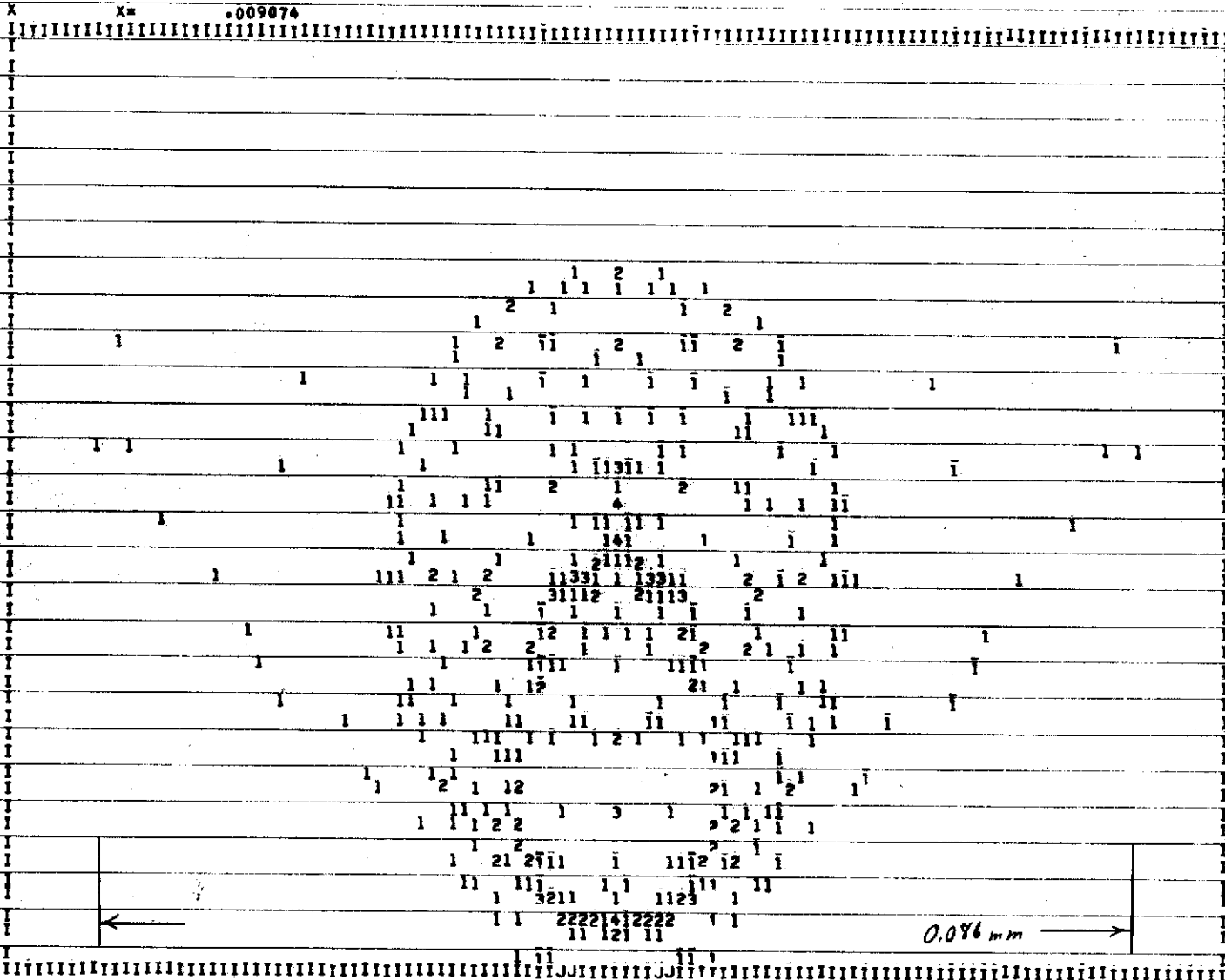


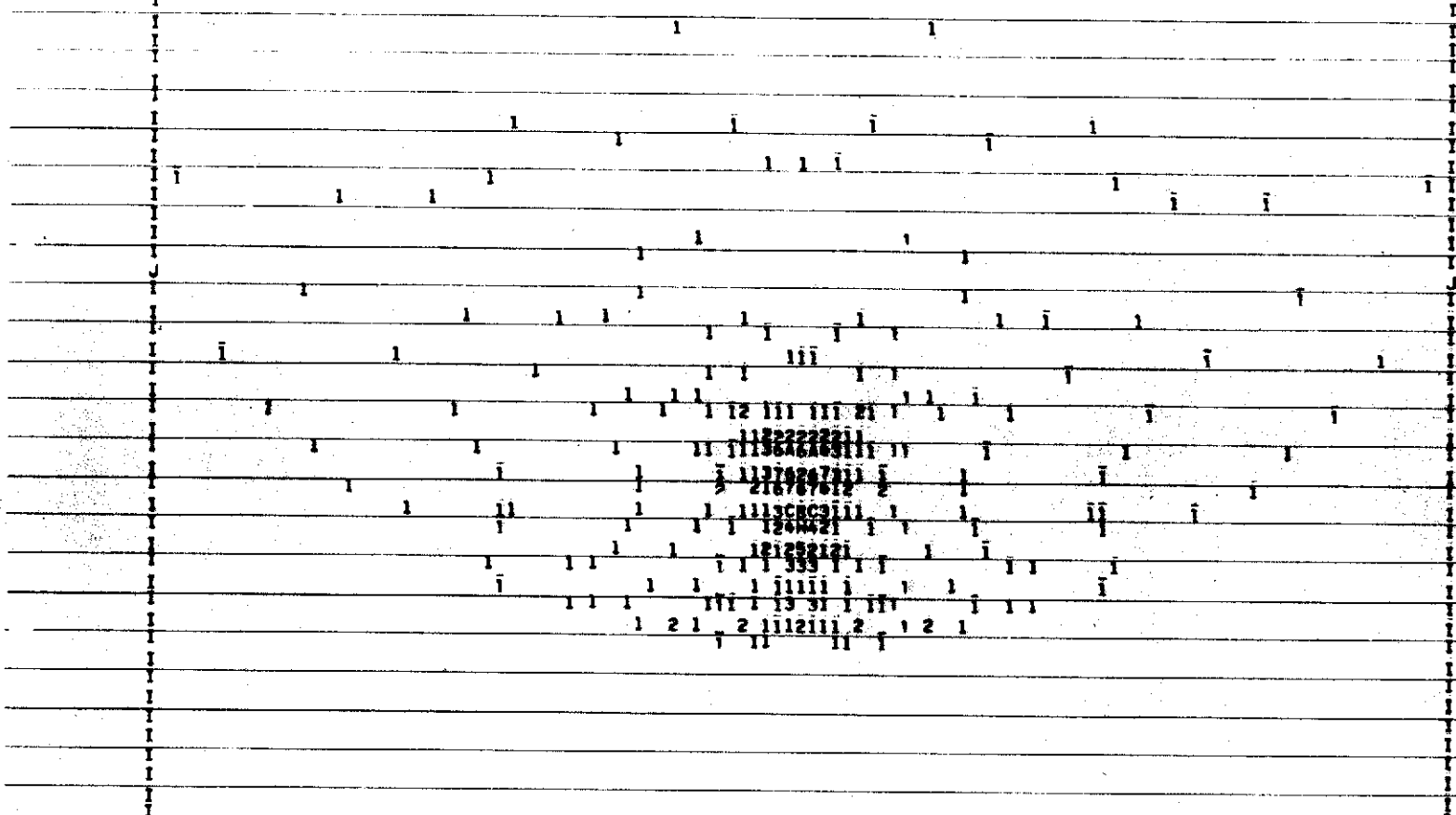
PLATE XXVII

WAVELENGTH = .60000 IMAGE HEIGHT = 3.9128
 FIELD 4 5 RAYS OUTSIDE 247 RAYS BLOCKED-OUT OF A TOTAL OF 729 RAYS

page 99

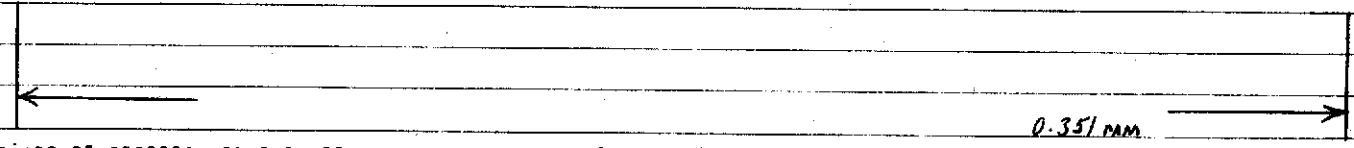
bob

X= .033070



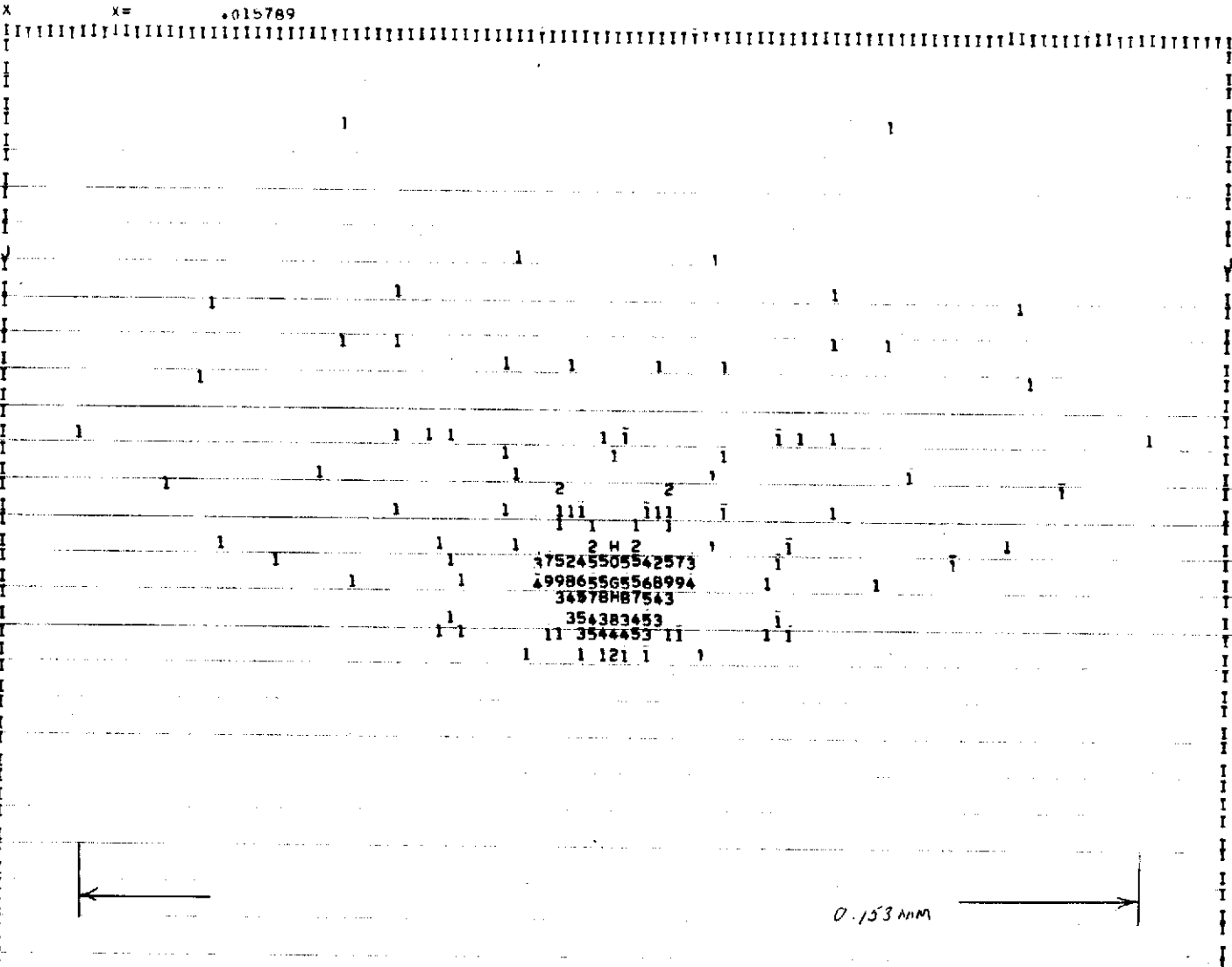
1152222811
 117926711
 216787612
 113080311
 120421
 121222121
 1111111
 1111111
 1111111
 1 2 1 2 1112111 2 1 2 1

100



WAVELENGTH = 4000 IMAGE HEIGHT = 5.2268
 FIELD 5 2 RAYS OUTSIDE 274 RAYS BLOCKED OUT OF A TOTAL OF 729 RAYS

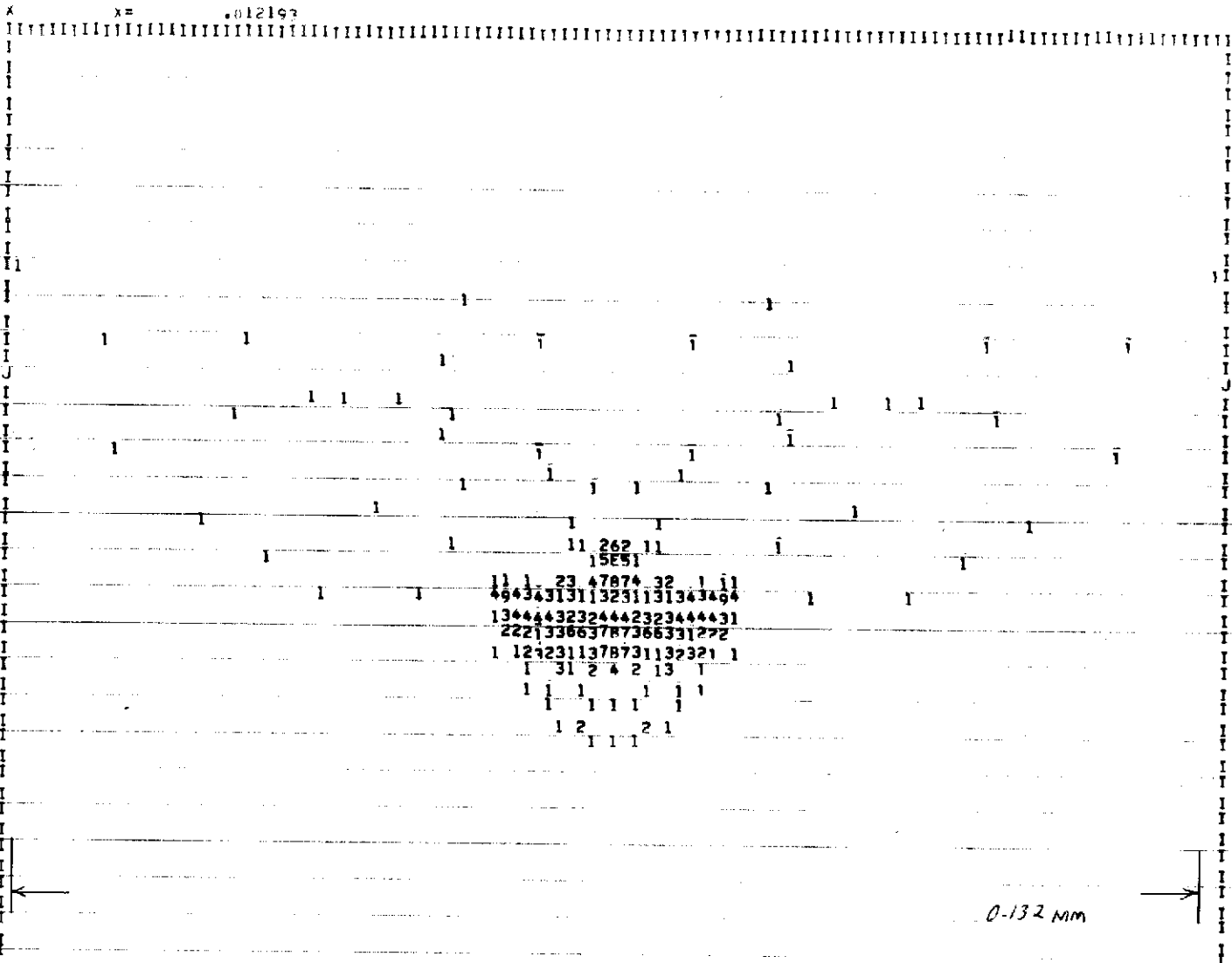
Page 100



WAVELENGTH = 4500 IMAGE HEIGHT = 5.2268
 FIELD 5 2 RAYS OUTSIDE 274 RAYS BLOCKED OUT OF A TOTAL OF 729 RAYS

101

page 101



WAVELENGTH# .47500 IMAGE HEIGHT# 5.2208
 FIELD 5 0 RAYS OUTSIDE 272 RAYS BLOCKED OUT OF A TOTAL OF 729 RAYS

Page 102

x= .010702

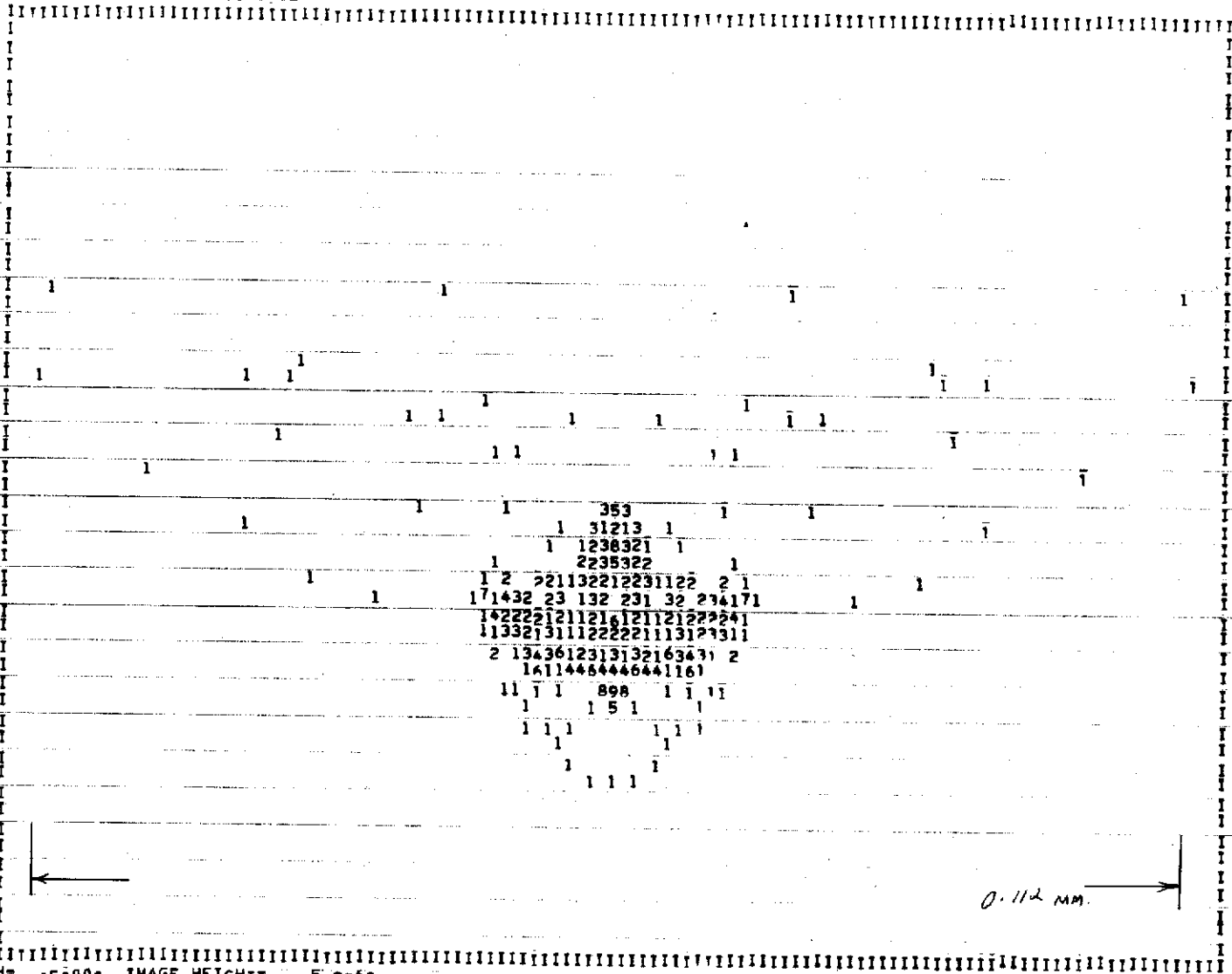


PLATE XXXI

0.112 mm.

WAVELENGTH= 5000 IMAGE HEIGHT= 5.2268
 FIELD 5 2 RAYS OUTSIDE 272 RAYS BLOCKED OUT OF A TOTAL OF 729 RAYS

Page 103

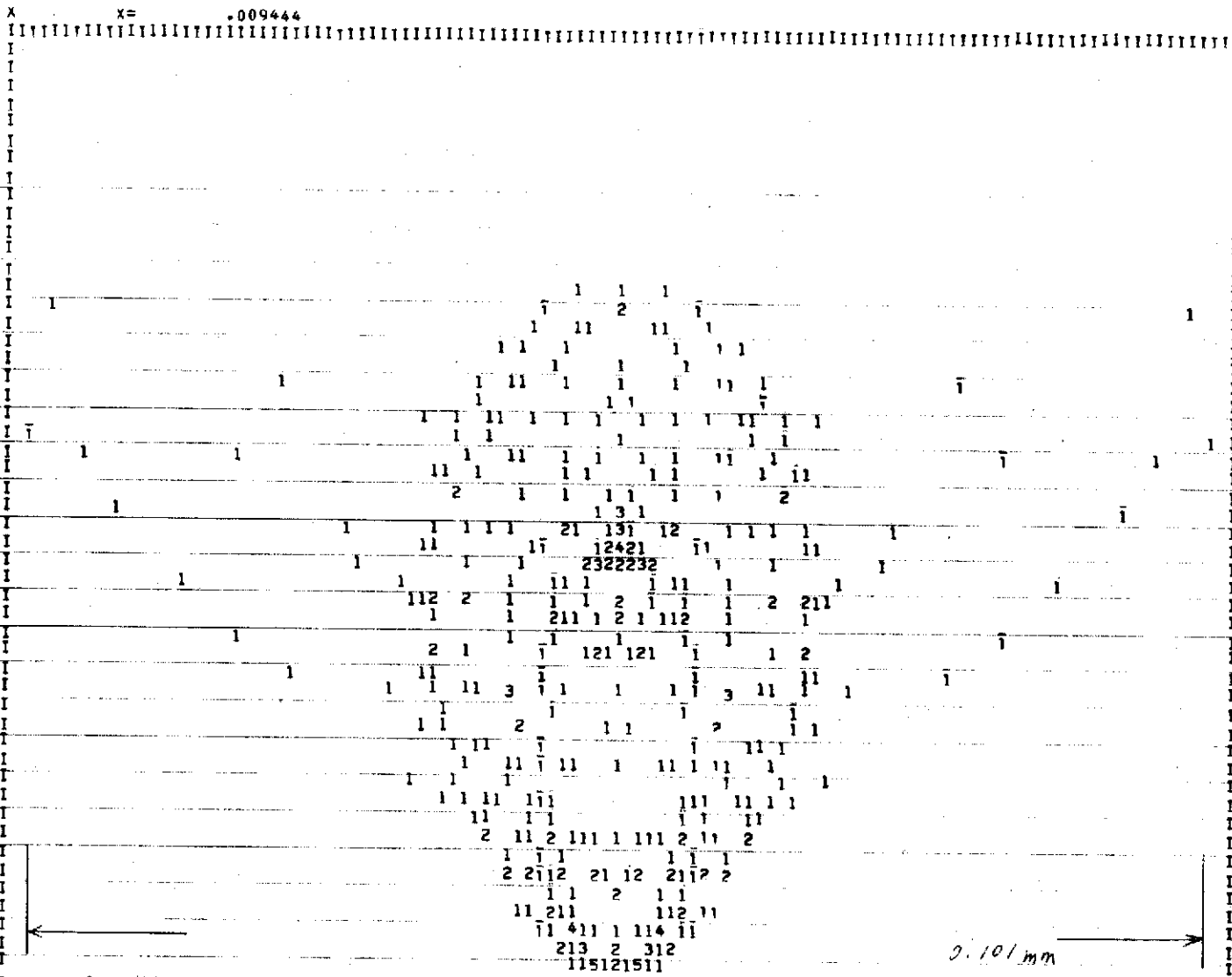


PLATE 35619

WAVELENGTH 6000 IMAGE HEIGHT 3.2268
 FIELD 5 0 RAYS OUTSIDE 274 RAYS BLOCKED OUT OF A TOTAL OF 729 RAYS

page 106

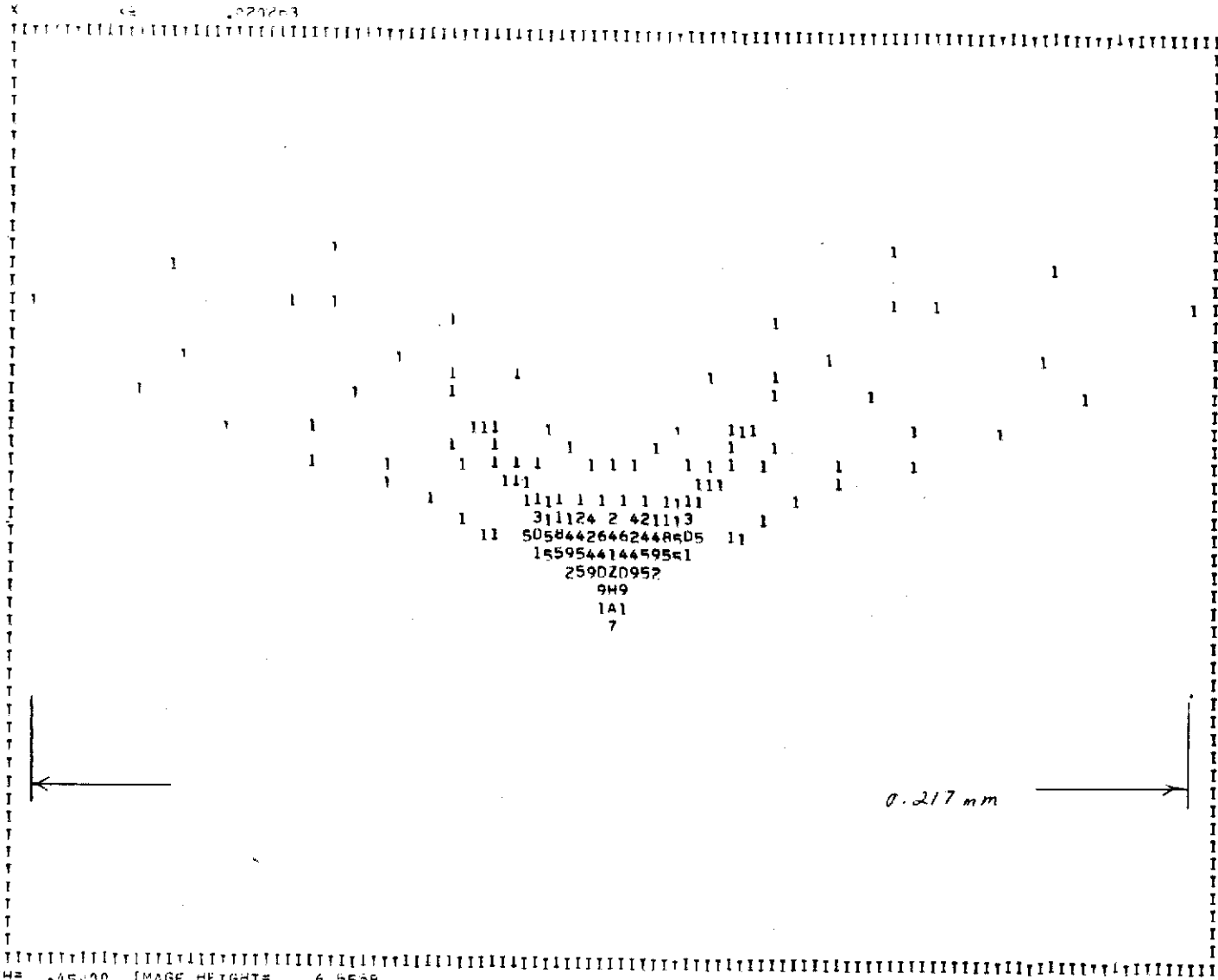
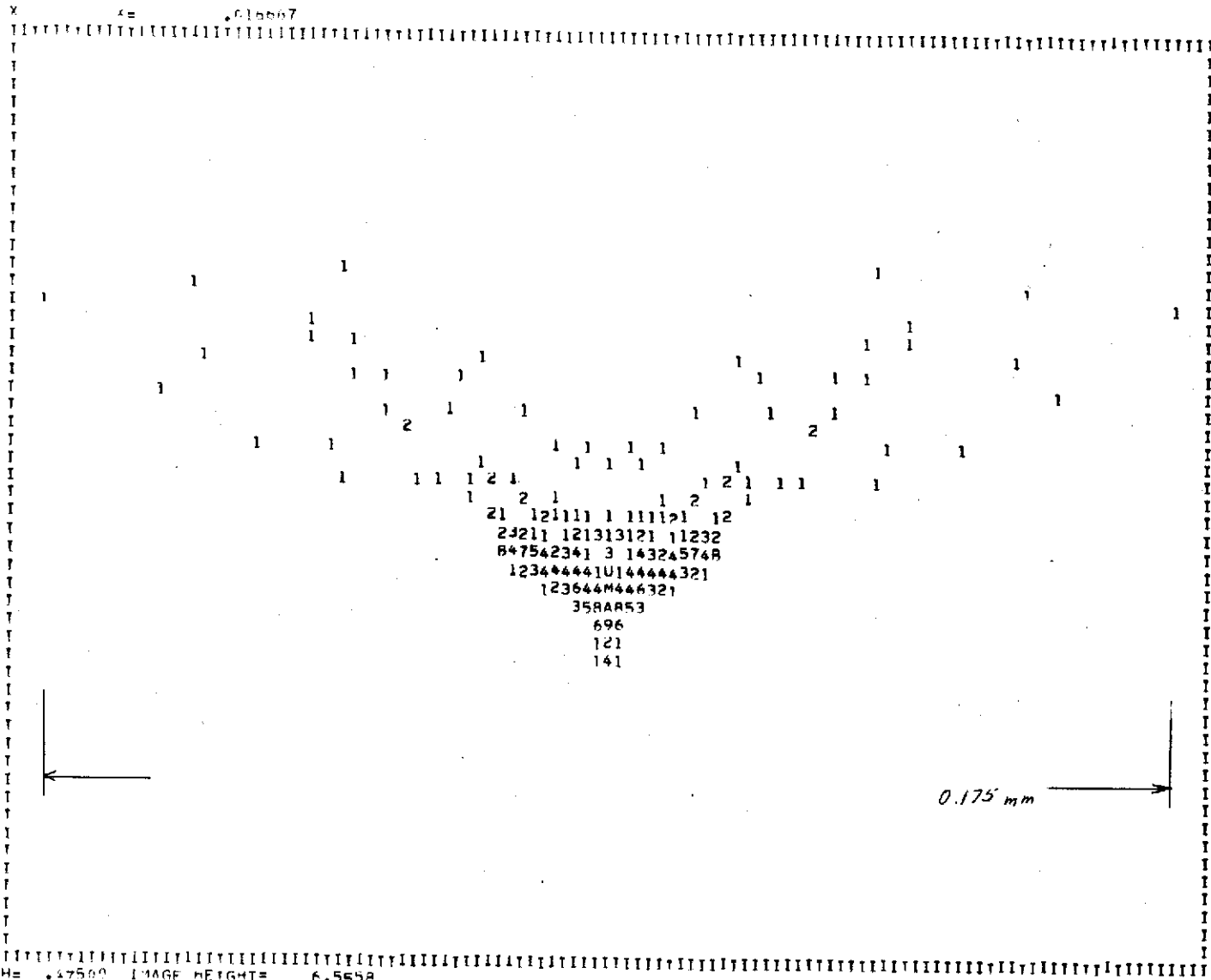


PLATE ~~XXXX~~

0.217 mm

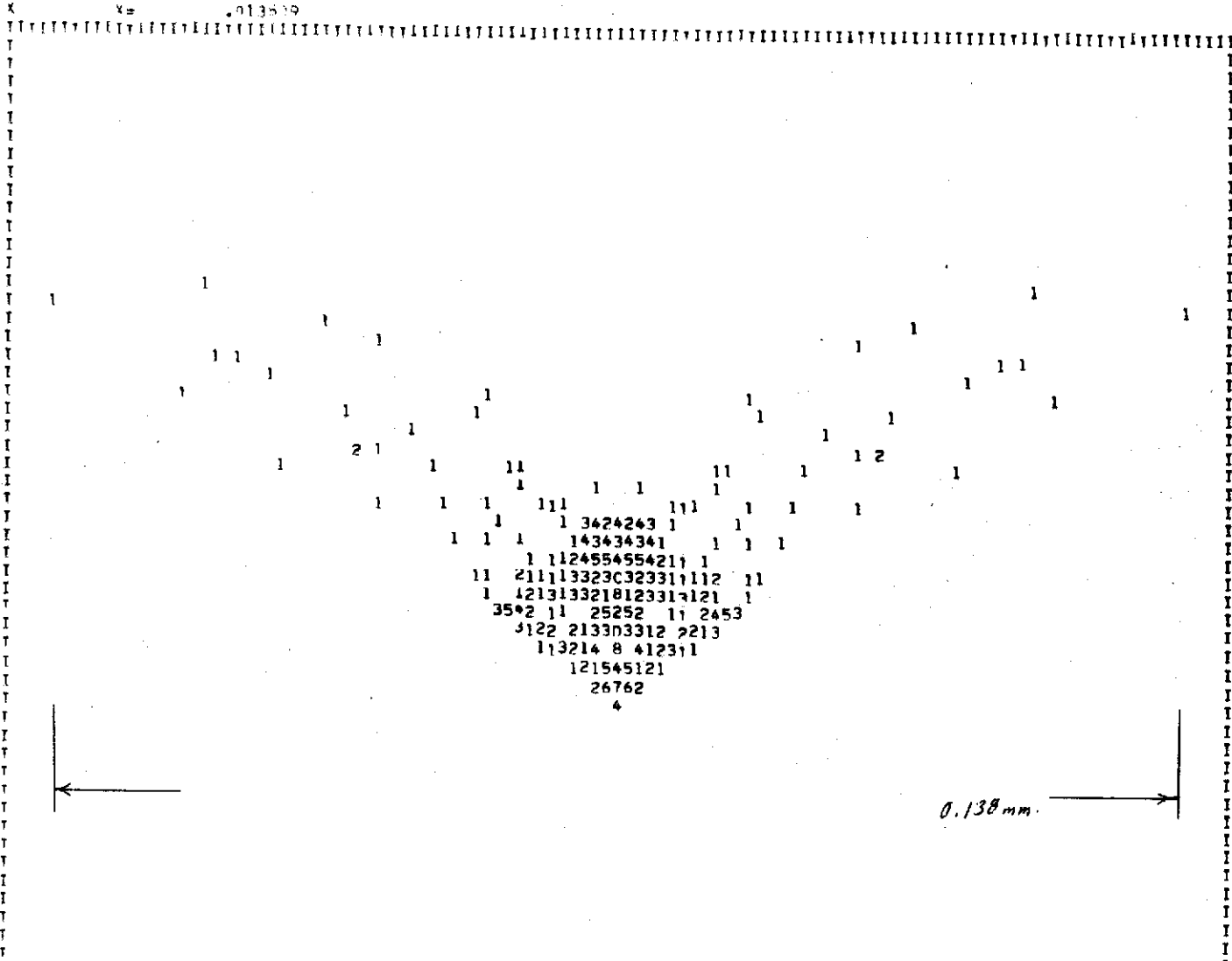
WAVELENGTH# 44500 IMAGE HEIGHT# 6.955P
 FIELD # 2 2 RAYS OUTSIDE 340 RAYS BLOCKED OUT OF A TOTAL OF 729 RAYS

page 108



WAVELENGTH= 0.68667 IMAGE HEIGHT= 6.555R
 FIELD 2 2 RAYS OUTSIDE 300 RAYS BLOCKED OUT OF A TOTAL OF 720 RAYS

page 109



1 1124554554211 1
 11 21113323032331112 11
 1 121313321812331121 1
 35*2 11 25252 11 2453
 1122 213303312 2213
 113214 8 412311
 121545121
 26762
 4

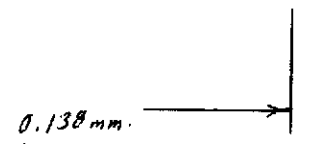
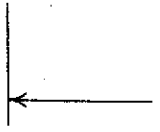


PLATE XXXX

WAVELENGTH .52500 IMAGE HEIGHT= 4.555A
 FIELD 2 2 RAYS OUTSIDE 302 RAYS BLOCKED UNIT OF A TOTAL OF 729 RAYS

Page 111

v = 011754

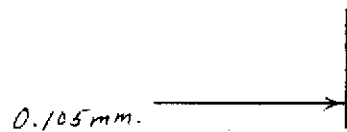
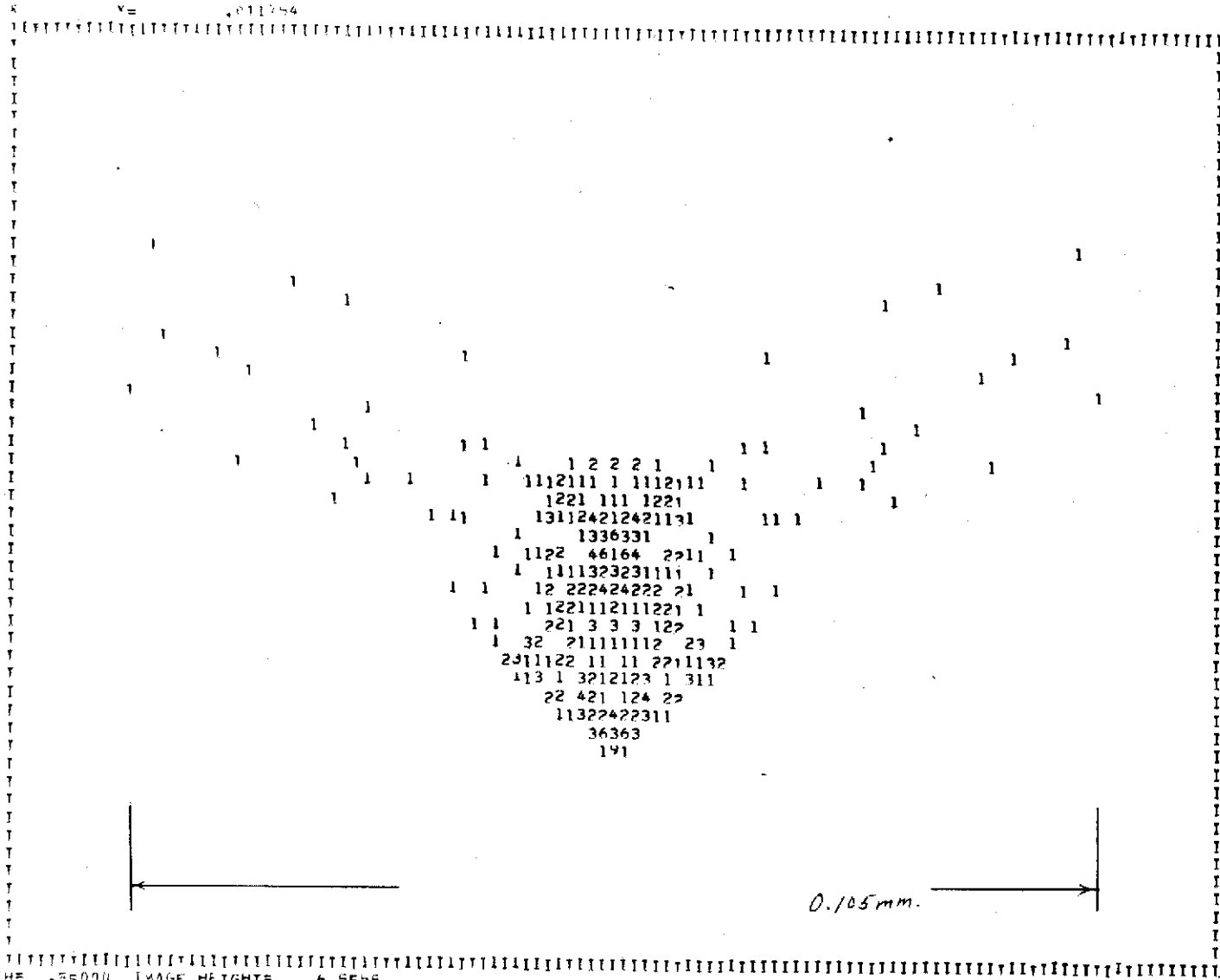


PLATE IV

WAVELENGTH 0.5500 IMAGE HEIGHT 6.955R
 FIELD 2 2 RAYS OUTSIDE 314 RAYS BLOCKED OUT OF A TOTAL OF 729 RAYS

Handwritten signature
 112

